

Simulating the Cluster satellites in a cold plasma flow
"A numerical study of spacecraft wake formation"

RAM PRAKASH

Swedish Institute of Space Physics / Technical University of Delft

July 10, 2007



INSTITUTET FÖR RYMDFYSIK
Swedish Institute of Space Physics

Uppsala, July 11, 2007

Approval

This is to certify that Mr. **Ram Prakash** (Technical University of Delft) has completed his internship period at the Swedish Institute of Space Physics in Uppsala. This document also constitutes the formal approval of his internship report, *Simulating the Cluster satellites in a cold plasma flow: A numerical study of spacecraft wake formation*, which he has completed to great satisfaction.

Anders Eriksson
Senior scientist, supervisor

Contact information:

Anders.Eriksson@irfu.se

Swedish Institute of Space Physics
P. O. Box 537
SE-751 21 Uppsala, Sweden

+46-18-4715945

<http://www.irfu.se>

Internship Report

done at the research group of

Space Plasma Physics

at

Swedish Institute of Space Physics (IRFU)

Submitted for approval on
July 10, 2007

Copyright © 2007
Ram Prakash, Delft, July 10, 2007.

This research has been carried out at:

Swedish Institute of Space Physics
P.O.Box 537, SE-751 21 Uppsala, Sweden.

This document was typeset with $\text{\LaTeX} 2_{\epsilon}$. Reproduction or translation of any part of this work in any form by print, photoprint or any other means, without prior permission of either the author or the research group is prohibited.

Contents

| | | |
|----------|---|-----------|
| 0.1 | Abstract | x |
| 0.2 | Acknowledgements | xi |
| 1 | Introduction | 1 |
| 2 | Swedish Institute of Space Physics | 3 |
| 2.1 | Overview | 3 |
| 2.2 | IRF Uppsala (IRFU) | 3 |
| 3 | Space Plasma | 5 |
| 3.1 | Plasma features | 5 |
| 3.2 | Plasma criteria | 6 |
| 3.3 | Plasma parameters | 6 |
| 3.4 | Space environment | 7 |
| 4 | Mathematical Modeling | 10 |
| 4.1 | Overview | 10 |
| 4.2 | Kinetic theory | 11 |
| 5 | Spacecraft-Plasma Interactions | 13 |
| 5.1 | Overview | 13 |
| 5.2 | Conductive object in plasma | 13 |
| 5.3 | Spacecraft charging | 14 |
| 5.4 | Wake formation | 15 |
| 6 | Method of Approach | 17 |
| 7 | Numerical Tools | 18 |
| 7.1 | Overview | 18 |
| 7.2 | Geometry and meshing | 18 |
| 7.3 | SPIS-Num | 21 |
| 7.4 | SPIS-UI | 23 |
| 8 | Sphere Simulations | 28 |
| 8.1 | Introduction | 28 |
| 8.2 | Passive sphere of radius 0.25 m | 28 |
| 8.3 | Passive sphere of radius 1 m | 32 |
| 9 | Cube Simulations | 33 |
| 9.1 | Introduction | 33 |
| 9.2 | Mass ratio | 33 |
| 9.3 | Real simulations | 34 |

| | |
|---|-----------|
| 10 Cylinder Simulations | 39 |
| 10.1 Introduction | 39 |
| 10.2 Simulations | 39 |
| 11 Boom Simulations | 45 |
| 11.1 Introduction | 45 |
| 11.2 Normal boom | 46 |
| 11.3 Inclined boom | 47 |
| 12 Conclusions | 53 |
| A Simulation Settings and Procedures | 56 |
| A.1 Before starting SPIS | 57 |
| A.2 After starting SPIS | 57 |
| A.2.1 Loading the geometry | 57 |
| A.2.2 Properties definition | 58 |
| A.2.3 Properties attribution | 59 |
| A.2.4 Meshing the geometry and group conversion | 60 |
| A.2.5 Global parameter settings | 60 |
| A.2.6 Post processing | 60 |
| A.2.7 Saving the project file | 61 |

List of Figures

| | | |
|------|--|----|
| 3.1 | Schematic view of heliosphere (<i>Kallenrode</i> ^[9]) | 7 |
| 3.2 | Schematic view of Earth's magnetosphere (<i>Kallenrode</i> ^[9]) | 8 |
| 5.1 | Ion and electron impact on an uncharged object (<i>Tribble</i> ^[2]) | 14 |
| 5.2 | Red path shows the orbit of Cluster (www.esa.int) in spring time. Half a year later, apogee is in the magnetic tail and perigee on the dayside | 15 |
| 5.3 | Wake formation - a) when the ion flow energy higher than the spacecraft potential and b) when the ion flow energy lower than the spacecraft potential (<i>Engwall, et.al</i> ^[8]) | 16 |
| 7.1 | Computational volume divided in to blocks and attached to the cube | 19 |
| 7.2 | Split view showing two of the blocks with 1D meshing | 20 |
| 7.3 | Numerical structure of SPIS code (<i>Roussel, et.al</i> ^[6]) | 21 |
| 7.4 | Spacecraft equivalent circuit with continuous components (<i>Roussel, et.al</i> ^[6]) | 22 |
| 7.5 | Spacecraft equivalent circuit with continuous and discrete components (<i>Roussel, et.al</i> ^[6]) | 23 |
| 7.6 | Top-level design of SPIS-UI (<i>Roussel, et.al</i> ^[12]) | 24 |
| 8.1 | Electron current collected Vs Time | 29 |
| 8.2 | Potential Vs Dimensionless radius | 30 |
| 8.3 | Potential decay from the sphere (Grid points in XY plane) | 31 |
| 8.4 | Electron density (Grid points in XY plane) | 31 |
| 8.5 | Collected electron current Vs time | 32 |
| 9.1 | Ion density around the cube for two different flow velocities | 35 |
| 9.2 | Ion density structure in XY plane | 36 |
| 9.3 | Potential obtained in the XY plane with a minimum value of -0.24 V (The equipotential contours are drawn for -0.24, -0.15, -0.05, -0.01, 0.01, 0.1, 0.5, 1 and 10 V) | 36 |
| 9.4 | Potential difference between the probes at different flow angles | 37 |
| 9.5 | Potential from simulation plotted with analytical potential distributions around a sphere | 38 |
| 10.1 | Ion density around the cylinder in various planes | 40 |
| 10.2 | Plasma potential around the cylinder in various planes | 41 |
| 10.3 | Potentials from simulations plotted with analytical potential distributions around a sphere | 42 |
| 10.4 | Potential difference between the probes at different flow angles | 43 |
| 10.5 | Potential decay along the X axis (distance in m) | 44 |
| 11.1 | Cylindrical representation of the real wire boom | 46 |
| 11.2 | Ion density around the normal boom in various planes | 48 |

| | |
|--|----|
| 11.3 Plasma potential around the normal boom in various planes | 49 |
| 11.4 Ion density around the inclined boom in various planes | 50 |
| 11.5 Plasma potential around the inclined boom in various planes | 51 |
| 11.6 Electron density around the inclined boom in XZ plane | 52 |
| A.1 Cylinder and far field boundaries | 56 |

List of Tables

| | | |
|------|--|----|
| 8.1 | General parameter settings for the simulation | 28 |
| 8.2 | Simulation settings for various test scenarios | 29 |
| 8.3 | Parameter settings for the simulation | 32 |
| 9.1 | Simulation parameters | 33 |
| 10.1 | Simulation parameters | 39 |
| 11.1 | Simulation settings | 46 |
| A.1 | Simulation parameters | 57 |
| A.2 | Global parameters | 60 |

0.1 Abstract

A good understanding of the spacecraft-plasma interaction is particularly important in the case of satellites intended for measuring the electromagnetic characteristics of the space environment. This would facilitate a prior estimate of the induced errors in onboard measurements so that the undisturbed true values can be deduced from that. Spacecraft, when in the regions of Earth's magnetospheric tail lobes and in the polar cap, encounter very tenuous plasma and become positively charged due to the photoelectron emission. In such an environment, the kinetic energy of ions wouldn't be sufficient to reach the spacecraft and instead the ion would flow around an equipotential surface from the spacecraft. This would result in an enhanced wake behind the potential obstacle, with dimensions far exceeding that of the spacecraft. The wake potentials would be much lower than the free stream potential, resulting in an erroneous measurement, if any of the instruments onboard happened to be inside the wake. A good proof for this is evident in the measurements made by Cluster satellites, where the EFW instrument has detected an apparent electric field. In this project, we have used the new open source simulation code SPIS (Spacecraft Plasma Interaction Software), to numerically simulate the spacecraft-plasma interaction. The results verified the existence of such an enhanced wake behind the satellite, while operating in the mentioned regions, and also show good agreement with the observational data from Cluster satellites.

0.2 Acknowledgements

I am greatly indebted to my very friendly and helpful supervisor, Dr. Anders Eriksson, for all the encouragement and motivation he has given me throughout the work. I thank him for introducing me to the subject of space plasma physics and making my internship time an exciting learning experience. A big thanks goes to Lars Daldorff for the many fruitful discussions and suggestions regarding the simulation results. Above that, for being a nice colleague whom I could always approach for help. Yuri Khotyaintsev is thanked for helping me out with all the initial troubles in running the code as well as all the trouble-shootings later (some times I was sort of disturbing him). I also thank Bertil Segerström for his help with the computer accounts and nice chats. I would also take this opportunity to thank all other staff and students at IRFU, who has provided me with a pleasant working environment during my stint. Finally, cheers for my wonderful flat-mate Peter Schmidt (don't dare to ask him about his subjects, mushrooms or alcohol if you want to catch the bus within next 15 minutes) for providing me a nice room and friendly atmosphere to stay.

Chapter 1

Introduction

The Sun is continuously expelling a stream of charged particles, i.e. plasma, out into the solar system. This charged stream is called solar wind but when it originates from stars other than Sun, it is called stellar wind. The high kinetic energy associated with this ejection is not well understood but it is presumed to have attained in part due to the high coronal temperature of the source. The solar wind possesses the plasma properties of high electrical conductivity so that the magnetic field lines of the Sun are carried along with it. The Earth is protected from this flux by the magnetosphere that acts like a sheath around the Earth, deflecting the plasma stream. Nevertheless, the solar wind can sometimes be strong enough to deform the Earth's magnetic field and it would in turn be noticeable in the form of geomagnetic storms and aurora.

There has been profound curiosity among the space scientists all over the world regarding the various astrophysical phenomena in and around the Earth's magnetosphere. This has culminated in numerous space missions devoted entirely for studying the magnetosphere and surrounding regions. The most recent of this kind is the Cluster mission, an ESA initiative, involving four satellites flying in formation around the Earth. The main objective of the mission is to investigate the interaction between the solar wind and the magnetosphere.

For proper interpretation of the measurements, it is necessary to understand the interaction between the spacecraft and surrounding plasma. The main consequent of this interaction is the spacecraft charging, which is explained in detail in chapter 5. This, if the charge distribution is uneven, would in turn cause electrical discharges hazardous to the critical components of spacecraft such as electrical thrusters, batteries etc. Also it creates spurious electric field in the surrounding plasma which would in turn affect the plasma field measurement by the onboard instruments. So it is necessary to have a priori estimate of the disturbance function to either avoid such discrepancies or extract the accurate data even in their presence.

In this project, carried out at IRF Uppsala, a numerical study has been performed for a qualitative as well as quantitative estimation of the interaction between a Cluster satellite and plasma using the open source plasma simulation code SPIS (Spacecraft Plasma Interaction Software). The main objective is to reasonably model the wake structure behind the positively charged spacecraft and to determine the potential in the wake. Another motive is to validate the code by simulating some theoretically known cases and to test the applicability towards real situations. The details of the code and the numerical settings are elaborated in chapter 7. Due to the time limitations, a simulation with the full Cluster geometry is not performed in this study.

In this report, chapter 2 gives a brief outlook on the research activities at Swedish Institute of Space Physics (IRFU). Space plasma physics and the mathematical basis of plasma motion are described in chapters 3 and 4. The plasma interaction with spacecraft is dealt with in chapter 5. In chapter 6, the method of approach chosen for the project work is ex-

plained. Chapter 7 gives an introduction to the numerical code, SPIS, and also the modeling as well as simulation settings employed. Chapters 8 to 11 present the details of simulations done for each case as well as the obtained results. Finally some conclusions are summarized in chapter 12.

Chapter 2

Swedish Institute of Space Physics

2.1 Overview

The Swedish Institute of Space Physics (Institutet för rymdfysik, IRF), founded in 1957, is a governmental research agency with a work force of about 110 employees. Its head office is situated in Kiruna with divisions at Umeå, Uppsala and Lund. The institute's primary tasks are oriented upon basic research, education and observatory activities in space physics, space technology and atmospheric physics. Each of the above offices is concerned with one or more specific areas of research which can be classified as:

- IRF Kiruna: Atmospheric physics, space plasma physics and measurements of charged particles.
- IRF Umeå: Space environment, propagation of infrasound in atmosphere and development of new methods for signal processing and data analysis.
- IRF Uppsala: Space plasma and theoretical plasma physics, measurements of electric fields and waves.
- IRF Lund: Modeling and prediction of space weather.

IRF has world wide acclaim for its contributions towards space research. It is an active partner in many of the international satellite projects such as Cassini, Cluster, Rosetta, Venus Express etc., to name a few. IRF has onboard instruments in these satellites and also its own satellite named Munin, which was launched in 2000. The research activities are aided by the data from these satellites as well as experiments done with ground based instruments provided by the large-scale international research facility EISCAT (European Incoherent Scatter Association) with radar stations in Tromsø, Kiruna, Sodankylä and Svalbard. Also it uses data from a global network of ionosodes, magnetometers and optical cameras, including its own facilities installed at Kiruna, Uppsala and Lycksele.

Apart from this, IRF also plays a significant role in the education sector. It works in close collaboration with many of the leading Swedish universities, thus providing opportunities for students to utilize its research resources for doctoral as well as post doctoral studies. Also it contributes to university education at both undergraduate and graduate level by offering many short time project works and courses for students.

2.2 IRF Uppsala (IRFU)

The IRF branch in Uppsala is integrated with the Department of Astronomy and Space Physics of Uppsala University. The main research activities undertaken here come under the

divisions of Physics in Space (PHISP) and Space Plasma Physics (RPF). The main concentration of PHISP group is on the fundamental aspects of space physics such as the studies on physical principles, laws and mechanics that determine Earth's interaction with its space habitat. The scientific issues are tackled with theoretical, experimental as well as numerical approach. Some of the specific areas of interest of this group are dynamical/turbulent processes in space plasma, generic electromagnetic wave based physics in space and full kinetic theory modeling and visualization of electromagnetic turbulence in magnetized space plasma.

The Space Plasma Research (RPF) group is focused on experimental research in space physics, utilizing the observational data from both onboard and ground based instruments. The current main subjects addressed by the group are solar wind plasma interaction with Earth's magnetosphere, study of solar wind control of magnetosphere topology and physical coupling between the ionosphere and magnetosphere. The experimental activities undertaken in this frame depend a lot on the data acquired from satellites. One such is the Cluster satellites, which is the backdrop of this project work presented in the following chapters.

Chapter 3

Space Plasma

3.1 Plasma features

From our intuitive understanding of worldly matter, we can say it falls into one of the categories of solid, liquid or gas. But if we consider the universal domain, which includes the interplanetary and interstellar mediums, then we have to resort to further extension of classification to include a fourth state of matter called plasma. Of course there exist laboratory plasmas, but they are technological rather than of natural origin. Plasma represents the existence of matter in ionized state. Thus about 99 percent of the known matter in the universe is dominated by plasma, indebted to the electromagnetic radiation from Sun and other stellar sources. Even a short description of plasma physics is outside the scope of this report but a brief flip-through of some of the important aspects are presented in this chapter so as to have an easy interpretation of the subsequent chapters.

Basically, plasma is formed when gas is heated to a temperature whereby the constituent electrons in an atom attain sufficient energy to escape from the binding force of the nucleus. Even though plasma resembles the gaseous state of matter, it has many unique features. The main feature of plasma is quasi-neutrality, i.e. the number of positive (ions) and negative (electrons) charges in a sufficiently large volume are nearly equal. This nature of plasma should not be confused with the concept of a neutral gas, where also the charges are in equal proportion. To give a deeper insight into the disparity, plasma can be defined as a gas where the electrons possess enough kinetic energy to overcome the attractive potential energy of ions and remain free whereas in neutral gases, the potential energy is greater resulting in the existence of atoms rather than free electrons and ions.

The presence of free charges i.e. ions and electrons, makes plasma electrically conductive. The motion of electric charges induces magnetic fields and also it interacts strongly with the external magnetic fields. The magnetic fields would in turn affect the motion of the charge particles. The whole interaction processes can thus be compared to a feedback loop system where by the particle motion creates electric and magnetic fields which adds up with the external fields and it in turn influence the particle dynamics. Thus the plasma dynamics is much more complex than that of a neutral gas.

Another characteristic feature is the influence of particle behavior on state variables. In a gas, the state of the system is dictated by particle collisions and all the particles behave identically resulting in same state properties and a Maxwellian velocity distribution. On the other hand, in plasma, the electrons, ion as well as neutral particles behave distinctly depending on their corresponding charges leading to instabilities and non uniform state property distribution. If we look in to the particle collisions, we can find that in a gas the primary candidates are binary collisions while three-body collisions are rare. In contrary the plasma particle collisions show a collective behavior where each one interacts with lots of other particles depending on their charge because of the prevailing electromagnetic forces.

3.2 Plasma criteria

Before going into the plasma parameters we need to revert to a more scientific explanation for the plasma state. For any matter to be called a plasma, it has to satisfy three important criteria namely, plasma approximation, bulk interaction and plasma frequency.

The plasma approximation refers to the distinct feature of collective behavior of plasma where the charged particles have to be very close to each other so as to ensure that each particle interact simultaneously with lot of neighboring ones rather than the closest particle as in the case of gas. Such a sphere of influence of a particle is called Debye sphere whose radius (Debye length) is expressed as:

$$\lambda_{D_{e,i}} = \sqrt{\frac{\epsilon_0 k T_{e,i}}{n q_e^2}} \quad (3.1)$$

where ϵ_0 is the permittivity constant, k the Boltzmann constant, $T_{e,i}$ the electron/ion temperature, n the plasma density and q_e the electron charge. The average number of electrons inside a Debye sphere is given by the plasma parameter, Λ and expressed as:

$$\Lambda = \frac{4n\pi\lambda_D^2}{3} \quad (3.2)$$

The plasma approximation criterion can now be reinstated as $\Lambda \gg 1$. This implies that the Debye sphere would then be densely populated causing collective electrostatic interactions be dominant over binary collisions.

The criterion of bulk interactions implies that λ_D is shorter than the physical size of the system so as to achieve quasi-neutrality. Since every local charge concentration in the domain would be Debye shielded, the processes in the bulk of plasma are more significant than at the edges.

Another plasma defining criterion is that the electron plasma frequency or the plasma oscillations of electrons should be higher than the electron neutron collision frequency so that emerging charges are shielded rapidly. The plasma frequency is given by:

$$\omega_{pe} = \sqrt{\frac{ne^2}{\epsilon_0 m}} \quad (3.3)$$

where m is the mass of the electron and e the electric charge.

3.3 Plasma parameters

The plasma parameters define the characteristics of plasma and some of the most important parameters are degree of ionization, plasma temperature, and density. The extent of interaction between plasma and the surrounding electric and magnetic fields depends on the parameters.

As mentioned before, plasma represents the ionized state of matter. Thus we can infer that the plasma characteristics depend on the degree of ionization, which quantifies the proportion of atoms that have gained or lost electrons. It is controlled mainly by the temperature and is expressed as:

$$\alpha = \frac{n_i}{n_i + n_a} \quad (3.4)$$

where n_i and n_a are number densities of ions and neutral atoms respectively.

One of the most important plasma parameters is the temperature, which is a measure of the thermal kinetic energy of a particle and typically expressed in electron volts (eV). Due to the comparatively low mass of electrons, kinetic energy of electrons is relatively lower than

that of ions. The thermal energy of electrons is therefore often greater than its drift energy. Due to their low inertia the electrons also attain thermal equilibrium among themselves much faster than with ions and neutral atoms. In thermal plasmas, the ions and electrons exist in thermal equilibrium. In contrary, ions and neutral atoms often have a much lower temperature than electrons in non-thermal plasmas.

Plasma density, usually defined as the electron density, plays a vital role in determining the degree of ionization as well as the potential. The condition of quasi neutrality prevails on scales larger than λ_D due to the good electrical conductivity and there it can be approximated that the negative charge density is equal to that of positive charges. Charge imbalances do occur within the scales of λ_D . A charge imbalance on a scale larger than λ_D would require typical energies in excess of $\frac{KT_{e,i}}{q_e}$, and are thus rare.

3.4 Space environment

The main source of plasma in solar system space is the hard core electromagnetic flux emanating from the solar corona called solar wind. It is a mixture of protons, electrons with small amount of neutral particles such as Helium and other solar constituents. The interior of Sun consists of extremely hot and dense plasma as a result of the fusion processes. The lowest part of the solar atmosphere, the photosphere and the chromosphere, are much colder, but the upper atmosphere, the corona, once again reaches temperatures of the same order as in the Sun's core. The corona is unstable to be blown away as solar wind, which has an average speed of about 450 km/s. The solar wind carries the magnetic field of the Sun along with it and due to the rotation of Sun this results in winding up the field lines, known as Parker spiral, forming a void in space filled with plasma and magnetic flux. Such a void formed by solar wind is the Heliosphere and it extends to about 100 A.U. The Heliosphere has a rather complex structure with no well defined boundaries. A schematic representation is shown in figure 3.1.

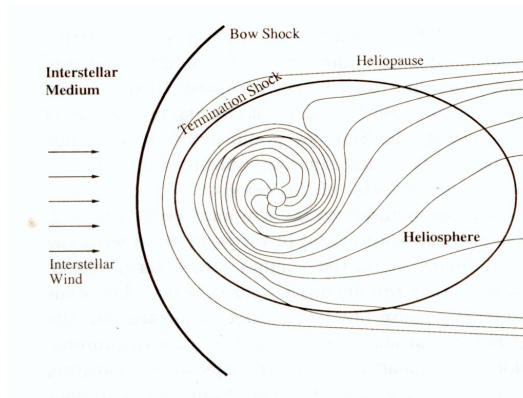


Figure 3.1: Schematic view of heliosphere (*Kallenrode*^[9])

The supersonically flowing solar wind from Sun is slowed down to subsonic values by the termination shock. Outside the termination shock the solar wind is affected by the incoming interstellar wind and a high pressure region is formed known as Heliosheath. The pressure of the stellar wind causes the Heliosheath to inherit a comet like shape extending away from the stellar wind direction. The boundary of Heliosheath (also Heliosphere) is called Heliopause, where the solar and interstellar mediums meet. The relative motion of the Sun and the interstellar medium results in advancement of Heliosphere towards the interstellar wind creating a turbulent region that terminates in a bow shock.

The interaction between solar wind flux and the planetary magnetic field creates voids also within the Heliosphere. There the particle motion is governed by the magnetic field of the concerned planet rather than that of Sun. In such a scenario, the energy density of the plasma is small compared with the energy density of field. Otherwise the particle motion would distort the field lines instead of the field lines guiding the particles. Such a region around a planet is termed as the planetary magnetosphere.

In case of Earth, the lower part of the magnetosphere is at distance of about 80 km, the starting point of ionosphere. The main contribution of plasma in ionosphere is by photo ionization. The entire ionosphere extends to a height of 1000 km but lies well inside the magnetosphere. The magnetosphere extends to about 10 Earth radii in the sunward side but goes well beyond the orbit of moon in the opposite direction. Close to the Earth, the geomagnetic field resembles a dipole with an orientation of approximately 15 degrees with respect to the geographic north. The schematic structure of Earth's magnetosphere is depicted in the figure 3.2.

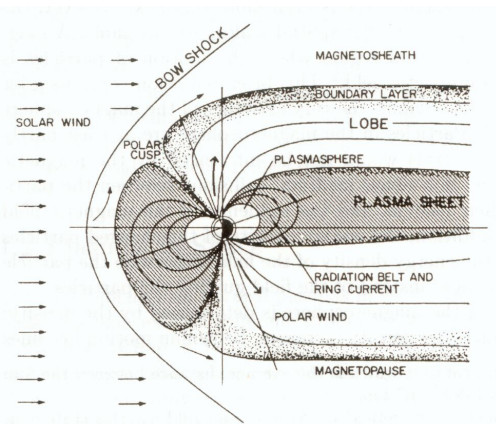


Figure 3.2: Schematic view of Earth's magnetosphere (*Kallenrode*^[9])

The incoming supersonic and super-Alfvénic solar wind is slowed down to subsonic values before hitting the Earth's magnetosphere by the bow shock. As the solar wind encounters the planetary magnetic field, currents are induced to resist the changes in its own magnetic field, thereby neutralizing the planetary field. This process is continued till the solar wind reaches the boundary of the magnetosphere, called magnetopause where the solar wind energy becomes unable to overcome the planetary magnetic field strength. It then gets deflected and flows around the magnetosphere to the downward side known as magnetosheath. The magnetopause is a reasonably well defined boundary where the transition is spontaneous, but has an internal structure as a region of pressure balance, and it can vary with the solar wind properties. The transition process is still a hot topic of research regarding whether the process is a smooth diffusion one or a sporadic rupture. The flow downstream of the bow shock causes the compression of magnetosphere in the sun-ward direction. Such a pressure imbalance is evident from the comet like appearance of the magnetosphere in downstream side; the low pressure and high velocity solar wind dragging the magnetosheath further down along with it.

Even though the magnetosphere acts like a sheath, a complete isolation from the solar plasma is not the case, thanks to the process of magnetic reconnection occurring in the polar cusp regions. In these regions, the solar magnetic field lines are oriented in the same way as that of their geomagnetic counterparts, thereby allowing a free flux transfer between the solar and terrestrial plasma regimes. Close to the Earth is a toroidal lobe, composed of particles in

eV range, known as plasmasphere. The distorted torus region next is called the plasmashet, comprising of high energy keV range particles making the plasma hot and dense. Above the plasmashet are the northern and southern tail lobes of magnetosheath with relatively cool and very diffuse plasma. This plasma mainly originates from the ionosphere, from which it flows out as the polar wind, a terrestrial analogue of the solar wind (though at lower temperature).

Chapter 4

Mathematical Modeling

4.1 Overview

Theoretically there are three but closely related approaches concerning the modeling of plasma. The first one is the particle orbit theory, where individual particles are tracked to determine its position and velocity in the prescribed electric (\mathbf{E}) and magnetic (\mathbf{B}) fields. In this no measure is taken to consider the origin of these fields, which can sometimes arise due to the collective motion of charges as well rather than some external means. Such an account is not possible with single particle motion, even though a time varying field employment is possible. This is also not a feasible one for implementing in numerical computations for the mere reason that there will be billions of particles in the computational domain. This has led to development of a fluid dynamic approach known as magnetohydrodynamics.

Magnetohydrodynamics can be called as the child born to fluid dynamics and electromagnetics. The plasma is modeled by a modified set of fluid dynamics equations that take into account the electro magnetic forces also. The main differences of this method from orbit theory are that it considers many particles instead of one and the \mathbf{E} and \mathbf{B} are not prescribed quantities but determined by the position and motion of particles. The later can be explained in a way that the particle motion generates the fields which then guide the motion of the particles. The fields can be externally applied also. So it requires both equations of motion and field equations to be solved simultaneously. Another characteristic of this approach is that it considers all the particles identically with same speed, temperature and a local Maxwellian distribution. In this way the thermal motion of particles are neglected. Such an approach is applicable in collision dominant plasma but it fails in collisionless cases where the particle distribution is predominantly non-Maxwellian, for e.g. inside a Debye sphere.

The quench for a wider applicability can be satisfied by resorting to the fundamental microscopic description of plasma known as the kinetic theory of plasma. In fact, the macroscopic properties can be derived by suitable averaging of the microscopic distribution function. Compared to gases, the main interaction between plasma particles is through Coulomb forces rather than collisions. These interactions are of long range and weak therefore the relaxation to a Maxwellian distribution is slow and many processes occur within this time scale. Here lies the utility of kinetic theory which is the topic of next section. A much detailed description of the mathematical foundations of all the three methods can be found in *Kallenrode*^[9] and *Dendy*^[11].

4.2 Kinetic theory

The kinetic theory is actually a statistical formalism of the plasma whereby the starting point is the individual particle physics and the macroscopic identities are derived by averaging over a large number of particles. The initial step in a kinetic description is the selection of a suitable distribution function depending on the time and length scales. The simplified approach is to employ a local Maxwellian distribution function with a particular temperature with length scale sufficient to contain many particles and on a corresponding small time scale. In such a way collisionless plasma can also be approximated.

Let $f_i = f_i(\mathbf{r}_i, \mathbf{v}_i, t)$ represents the distribution function of particle species i (ions and electrons) in six-dimensional phase space, where \mathbf{r} and \mathbf{v} are the position and velocity vectors. The spatial density of the species is then obtained by integration of the function over all velocities.

$$n_i(\mathbf{r}_i, t) = \int_{-\alpha}^{\alpha} f_i(\mathbf{r}_i, \mathbf{v}_i, t) d^3\mathbf{v}_i \quad (4.1)$$

The charge density of the species, which is product of spatial density and corresponding charge (q), follows from equation 4.1 and is given as:

$$\rho_i = q_i n_i \quad (4.2)$$

The heart of kinetic theory is the Boltzmann equation which is the fundamental equation of motion of a particle under the influence of external forces. The general form of the equation includes a collision term but collisions are rare in space plasma so we can use the collisionless Boltzmann equation, expressed as:

$$\frac{\partial f_i}{\partial t} + \mathbf{v}_i \cdot \frac{\partial f_i}{\partial \mathbf{r}_i} + \mathbf{a}_i \cdot \frac{\partial f_i}{\partial \mathbf{v}_i} = 0 \quad (4.3)$$

where \mathbf{a} is the acceleration.

In equation 4.3, the term \mathbf{a} determines the forces acting on the particle. For the present plasma state, the only forces acting are the electromagnetic ones as there is no collision interaction. The force that influences the particle motion under local electric and magnetic fields is the Lorentz force, expressed as:

$$\mathbf{F}_i = m_i \mathbf{a}_i = q_i (\mathbf{E} + \mathbf{v}_i \times \mathbf{B}) \quad (4.4)$$

where \mathbf{F} is the force acting on the particles, m the mass, \mathbf{E} the electric field and \mathbf{B} the magnetic field. Combining equations 4.3 and 4.4 gives the Vlasov equation, which defines the motion of a particle under the influence of an average Coulomb field generated by the motion of other particles in the domain, the very essence of plasma interaction. It is expressed as:

$$\frac{\partial f_i}{\partial t} + \mathbf{v}_i \cdot \frac{\partial f_i}{\partial \mathbf{r}_i} + \frac{q_i}{m_i} (\mathbf{E} + \mathbf{v}_i \times \mathbf{B}) \cdot \frac{\partial f_i}{\partial \mathbf{v}_i} = 0 \quad (4.5)$$

The above equations (4.1-2 and 4.4-5) are complimented by the Maxwell's set of equations; a conglomeration of Poisson equation, Gauss's law, Faraday's law and Ampere's law, as follows:

$$\text{Poisson equation : } \quad \nabla \cdot \mathbf{E} = \frac{\rho}{\epsilon_0} \quad (4.6)$$

where the total charge density (ρ) = $\sum_i \rho_i$ and ϵ_0 is the absolute permittivity (value in S.I. units is 8.854e-12 F/m). A non rotational central force field can be expressed as the gradient of a scalar potential. Thereby putting $E = -\nabla\Phi$, where Φ is the scalar electric potential, equation 4.6 becomes $\nabla^2\Phi = -\frac{\rho}{\epsilon_0}$.

$$\text{Gauss law : } \quad \nabla \cdot \mathbf{B} = 0 \quad (4.7)$$

$$\textit{Faraday's law} : \quad \nabla \times \mathbf{E} = -\frac{\partial \mathbf{B}}{\partial t} \quad (4.8)$$

$$\textit{Ampere's law} : \quad \nabla \times \mathbf{B} = \mu_0 \mathbf{J} + \epsilon_0 \mu_0 \frac{\partial \mathbf{B}}{\partial t} \quad (4.9)$$

where \mathbf{J} is the current density and μ_0 the absolute permeability (value in S.I. units is 1.256×10^{-6} H/m). The above equations form a set of non-linear equations in six dimensional space describing the motion of plasma particles under electro magnetic forces without collision. The detailed mathematical definitions and derivations can be found in *Kallenrode*^[9] and *Dendy*^[11].

Chapter 5

Spacecraft-Plasma Interactions

5.1 Overview

The major aspect of concern in any attempt for an accurate estimation of the electric field measurements in a space environment arises from the interaction between spacecraft and the plasma. The main consequences of these interactions are spacecraft charging, which if uneven and reaching sufficiently high voltages would be hazardous to the spacecraft and its components, and the perturbation in actual plasma potential around the spacecraft that would then affect the field measurements taken by the instruments onboard. The charging is becoming more of a concern with the integration of complex active devices such as electric thrusters and high voltage solar arrays. The problem of uneven charging is not of serious issue in Cluster satellite as it is built with a conductive surface. So potentials generated don't impact the satellite structure very much. On the other hand, they are of utmost relevance to the perturbation of surrounding plasma. In missions where accuracy is demanded at its best, a small potential on the spacecraft can disturb the plasma potential around it, botching the accuracy of measurements.

Before going deeper into the issue of charging in a Cluster satellite we will discuss some of the fundamental concepts in the next two sections of this chapter. A rigorous study into the various factors of charging and perturbation is outside the scope of this work, but some of the general aspects are discussed here. A detailed explanation as well as the mathematical basis can be found in *Tribble*^[2].

5.2 Conductive object in plasma

A conductive object immersed in plasma would be subjected to an unequal flux of ions and electrons, inducing a net charge, due to the variation in their respective thermal speeds. The thermal speed of electrons is higher than that of ions, so they hit the object more frequently. Moreover, generally the electron thermal velocity is much greater than the relative velocity of plasma (especially within the orbital path of Cluster satellite), whereas it often is lesser of ions. This causes the ions to impact mostly on the face normal to the velocity vector while the electrons can reach the entire surface area of the object. This situation, known as mesosonic flow (subsonic with respect to electron thermal speed, supersonic with respect to ion thermal speed), is the target of the present study. The collection of current is depicted in figure 5.1.

The ion and electron currents collected by an object at negative potential V in a mesosonic flow are expressed as:

$$I_i = qn v_0 A_i \left(1 - \frac{2qV}{mv_0^2} \right) \quad (5.1)$$

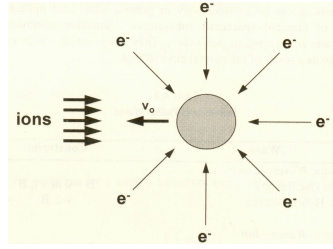


Figure 5.1: Ion and electron impact on an uncharged object (*Tribble*^[2])

$$I_e = \frac{1}{4}qn \left(\exp\left(\frac{qV}{kT_e}\right) \right) v_{e_{th}} A_e \quad (5.2)$$

where I_i and I_e represent the ion and electron currents respectively, q is the elementary charge (or electron/ion charge, always counted positive), v_o the plasma drift velocity, $v_{e_{th}}$ the electron thermal velocity, V the potential of the immersed object (equal to zero for an uncharged object), A_i the ion collecting area that depends on orientation in case of asymmetric shapes and A_e is the electron collecting area.

Due to the more frequent hitting of electrons, the body gets charged to high negative potentials until it reaches a value where the ion and electron current balance. Such a potential is called the floating potential, obtained by equating the above equations and given as:

$$V_{fl} = \frac{kT_e}{q} \ln\left(\frac{4v_o A_i}{v_{e_{th}} A_e}\right) \quad (5.3)$$

However, the above expression doesn't include the effects of secondary currents arising from photo emissions, secondary emissions and backscattering. The photoelectric current is caused by the emission of electrons when a material is exposed to light of sufficient energy to liberate the surface electrons. Secondary electron emission occurs when ions or neutrals impact the material with high kinetic energy strong enough to break the electrical attraction of electrons to the surface. If the immersed object or material is charged to high negative/positive potentials greater than the drift energy of the incoming plasma, it would result in back scattering of the electrons/ions. Moreover some spacecrafts are equipped with an active ion source such as ion thrusters that would contribute to the charging. So a more general expression applicable to a spacecraft is as follows (*Engwall*^{[4],[3]}):

$$I_e - (I_i + I_{bse} + I_{se} + I_{si} + I_{ph}) + I_b = 0 \quad (5.4)$$

where I_i and I_e are the incident ion and electron currents respectively, I_{bse} the backscattered electron current due to I_e , I_{se} and I_{si} are the secondary emission current due to electrons and ions respectively, I_{ph} the photoemission current and I_b the current from an ion source. Though the above equation takes into account the main current inducing phenomena, it omits many of the low magnitude effects such as field-aligned currents (due to variation in current collection along and across the magnetic field lines), ion focussing (associated with metallic interconnections and pinholes in the collection area) etc.

5.3 Spacecraft charging

The electrostatic potential attained by the spacecraft significantly alters the measurements made by electric field instruments. A proper understanding and estimation of such interferences are necessary for extracting the undisturbed distribution function from the measurements. A spacecraft can charge to negative or positive potentials depending mainly on the

plasma and sunlight characteristics at its orbital position and to a lesser extent on its surface properties. In line to the discussion in the previous section, a conductive object immersed in dense plasma can charge to high negative potentials due to the higher thermal energy associated with electrons. When dealing with space plasma, such a picture of dense plasma comes only if we are interested in ionospheric regions. Within the magnetosphere and in the solar wind the plasma is predominantly tenuous except within the plasma sphere, which is filled with cold dense plasma. In dense regions and also at any time when the spacecraft is in the Earth's shade, the spacecraft potential can reach to negative values of few times the electron temperature in magnitude. However for tenuous plasma, the dominant current would be that due to photoelectron emission, causing the spacecraft charge to high positive potentials.

One of the major dynamic effects is the formation of a wake behind the spacecraft. The supersonic flow of tenuous plasma around a spacecraft causes a wake to form behind it. When the relative speed exceeds the ion thermal velocity but not the electron thermal velocity, the wake gets negatively charged due to the thermal motions of electrons. This negative charge would then affect the field instruments when it happens to be inside the wake. Another effect is the occurrence of an apparent sunward electric field due to the asymmetries in photoelectron emission. These two effects are very much dependant as the photoelectron emission charges the spacecraft to positive potentials which would then dictates the local electric fields as well as the charge and size of the wake.

5.4 Wake formation

In case of a Cluster satellite, the perigee of its orbit is at around 4 Earth radii, and lies just outside the plasmasphere. The outer boundary of plasmasphere is unstable owing to the geomagnetic activity so that when in perigee the spacecraft occasionally experiences dense plasma flow around it, leading to negative spacecraft potential with respect to the surrounding plasma. So, in its orbit, a Cluster spacecraft passes through three different regions of plasma characteristics, presenting three distinct wake features. The three regions are plasmasphere, terrestrial magnetosphere (particularly the polar cap and tail lobe regions of Earth's magnetosphere) and the solar wind. The sketch of the orbital path is shown in figure 5.2.

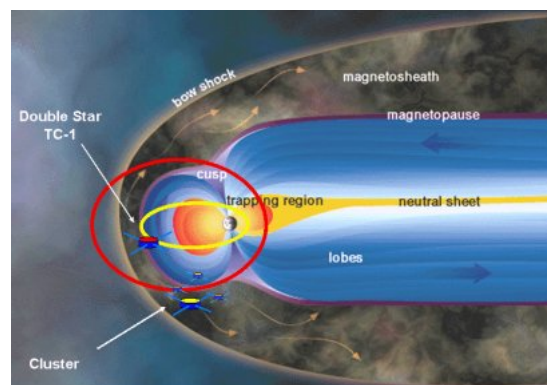


Figure 5.2: Red path shows the orbit of Cluster (www.esa.int) in spring time. Half a year later, apogee is in the magnetic tail and perigee on the dayside

In the ionosphere, the region around the perigee altitude, the potential of the spacecraft can reach negative values. This situation has been resorted to considerable amount of research and the results concluded that the spacecraft potential as well as negative wake

augments the filling up of ions in to the wake. So a stable wake structure is not the case in this region. The mathematical criteria for a stable wake to form are expressed as:

$$\text{Narrow wake : } KT_i < qV_{sc} < m_i \frac{u^2}{2} \quad (5.5)$$

$$\text{Enhanced wake : } KT_i < m_i \frac{u^2}{2} < qV_{sc} \quad (5.6)$$

where KT_i is the ion thermal energy, $m_i \frac{u^2}{2}$ the ion kinetic energy and qV_{sc} the spacecraft potential in electron volts.

In the solar wind, the region around the apogee altitude, the plasma is so tenuous (typically 5 cm^{-3}) that the electron current is much smaller than the photoelectron current. This would lead to positive spacecraft potentials of the order 5-10 V. This is greater than the ion thermal energy but much smaller than the kinetic energy of ions (typically 1 keV). So in this case the wake structure is determined by the physical geometry of the spacecraft rather than its potential. The figurative representation of such a wake is shown in figure 5.3.a.

The third regime is that of the terrestrial magnetosphere, where the plasma is much tenuous (around 0.1 cm^{-3} or less). In this region, the photoelectron emission dominates the electron collection current very much and as a result the potential of the spacecraft can reach up to high values of about 50V or more. The ion kinetic energy remains at a lower value of about 10 eV. In such a scenario, the wake structure is determined not by the physical structure of the spacecraft but rather by the equipotential surface, whereby the ions get scattered by the repulsive decaying potential from the spacecraft. This is shown in fig 5.3.b.

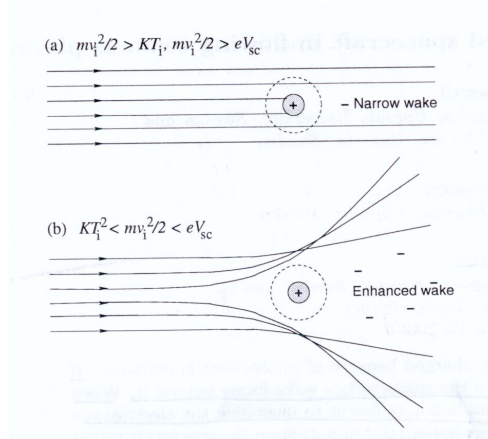


Figure 5.3: Wake formation - a) when the ion flow energy higher than the spacecraft potential and b) when the ion flow energy lower than the spacecraft potential (*Engwall, et.al*^[8])

Chapter 6

Method of Approach

While employing a new code for simulations, it is inevitable to initially validate the code by performing some test cases, whose solutions are known either analytically or numerically. Such an approach is followed here whereby the simulations done by *Roussel, et.al*^[5] are redone to compare the solutions. A step by step approach towards the real spacecraft geometry is followed so as to make sure of the accuracy of the modelling and parameter settings.

The test geometries are then replaced by cube geometry, approximating the spacecraft body and similar to the simulations done by *Engwall*^[3]. Numerous computations are performed to examine the effects of boundary conditions as well as the simulation box size. Two other parameters put through investigation are the average number of particles-in-cell and the ratio of largest to the smallest cell volumes. The influences of these settings are explained in detail along with the results presented in relevant sections. The geometry is then modified to the real spacecraft dimensions to estimate the body interference on the surrounding plasma. The influence of various boundary conditions is also examined for this case.

In the thesis work of *Engwall*^[3], the results of simulating a boom in plasma flow using PICUp3D code are presented. This is reevaluated here using SPIS and also a simulation done for boom orientation normal to the flow. To avoid the meshing complications in modelling a thin wire boom, the wire is modelled as a cylinder with an equipotential surface interpolated from the real wire potential at the centre. Due to the limited availability of time, a simulation on the full Cluster spacecraft geometry is not done but some discussions are included in the conclusions.

Chapter 7

Numerical Tools

7.1 Overview

The simulations are performed using the new code, Spacecraft Plasma Interaction Software (SPIS), developed in the frame of Spacecraft Plasma Interaction Network (SPINE) with support from ESA. The main objective behind the development of SPIS has been to materialize an open source, homogeneous, adaptable and extensible numerical tool to model and simulate the kinetic processes involved in spacecraft plasma interactions. Such a tool should incorporate complex pre as well as post processing phases within a user friendly environment. The requirements of adaptability and extensibility envisaged the need to follow an object oriented approach offered by modern languages such as Java and Python/Jython.

SPIS code is mainly a Java and Jython based framework, being interfaced with available open source tools for CAD modelling, meshing, post processing and graphical display. Currently the only modelling and meshing tool integrated with SPIS is Gmsh, an automatic three-dimensional mesh generator with built-in CAD and post processing facilities. There are two graphical display tools integrated with the SPIS, Cassandra and Paraview, though in the version (3.1.01) used for our simulations, only Paraview was functional. There are also in-built basic 2D and 3D viewers, but they are of little use in advanced post processing. In our case the 2D plots of the results are generated using Matlab while the 3D displays are obtained using Paraview. The core of SPIS, SPIS-Num, allows the modelling of plasma dynamics and its coupling with the spacecraft. The user interface module, SPIS-UI, provides the functional link between all the tools used along the simulation chain from the pre processing phase to the post processing part.

In the following sections, we will discuss some of the modelling problems encountered as well as the settings employed in each of the simulation phases, from geometry creation to output displays, along with a brief outlook in to the features as a starting. The constructive aspects of the tools are well explained in *Roussel, et.al*^{[1],[5],[12],[6]} and *Gauzaine, Remacie*^[7].

7.2 Geometry and meshing

Gmsh is an automatic 3D finite element mesh generator and is built around four modules: geometry, mesh, solver and post-processing. The geometry creation follows a bottom-up approach with a hierarchical order of points, lines, surfaces and volumes. Gmsh can generate only unstructured mesh and it also follows the bottom-up approach as that of geometry so that the mesh on a geometrical entity is constrained only by that of its boundary. An important feature of Gmsh is its ability for contextual mesh definitions such as to specify the adaptive meshes along the lines and surfaces. Such an adaptive mesh would then override the characteristic mesh length, if specified (otherwise default value of 1), of the boundary

points. The solver and post processing parts of Gmsh are not discussed here as we haven't used them for our simulations.

One of major strengths of Gmsh cannot be well utilised when interfaced with SPIS. The adaptive mesh specification is not recognized by SPIS so geometry with such mesh attributes could not be loaded. While meshing the computational geometry, it is desirable to have smaller cell sizes closer to the spacecraft/boom so as to smoothly resolve the potential decay, which diminishes slowly with distance closer to the structure. At far-field boundaries it is appropriate to keep large cell sizes as there are no strong gradients involved and also to balance the total number of cells in the computational volume. In Gmsh, such mesh sizes can be provided by specifying the characteristic mesh lengths (the length to the nearest node) while creating the basic entity, i.e. points, which make the lines and from lines to surfaces and then to volumes. But this would result in uneven meshing of the computational volume such as over refining of some of the space near the boundaries or under refining of some areas closer to the physical structure. Just by fiddling with the characteristic length wouldn't give any user control over the mesh and a smooth transition from lower to larger cell size is not attainable.

To overcome this difficulty, a block meshing is employed for modelling the computational volume. In this, the total volume around the structure is divided into blocks, each having one boundary surface coinciding with one of the faces of the structure and another surface that with one of the outer boundaries of the computational box. The lines joining these two faces would then inherit the characteristic length of the structure at one end and that of the outer boundary at the other end. In such a way a smooth transition of smaller node lengths, at the inner end, to the larger node lengths at outer end can be obtained. This facilitates a similar meshing pattern in surfaces as these are generated from the line meshes, and then to each volumes. The division of the computational volume in to blocks are illustrated in figures 7.1 and 7.2. In figure 7.2, we can see the incremental progression of the node lengths

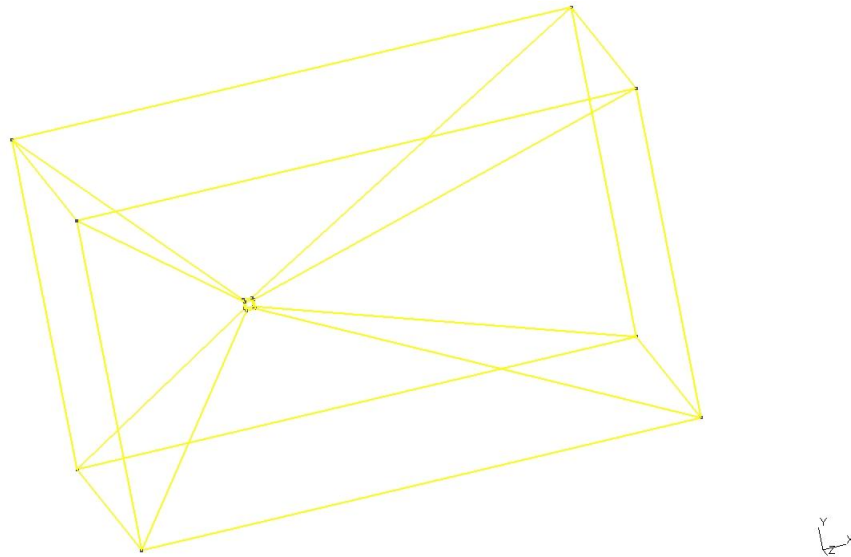


Figure 7.1: Computational volume divided in to blocks and attached to the cube

from the inner surfaces to the outer boundaries.

Even though the user can control the meshing as explained above, there is a limiting factor concerning the cell sizes when the geometry is used in SPIS. This is the ratio of largest to the smallest cell volume, owing to the particle-in-cell (PIC) model employed in SPIS for solving

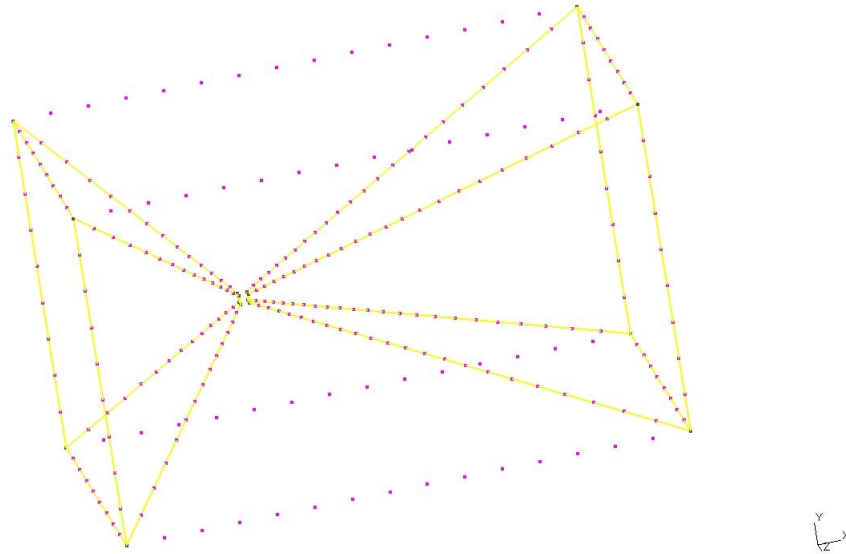


Figure 7.2: Split view showing two of the blocks with 1D meshing

the non-linear set of equations described in section 4. In PIC model, the motion of plasma particles under the influence of electric and magnetic fields are traced. In order to reduce the computational time, it is not the motion of individual particles but that of macro particles are traced. The basic model implemented for particle trajectory integration is a leap frog scheme and the charge densities at each nodes of a cell are evaluated from the particle charge through a linear weighting. A macro particle constitutes a large number of real particles, whose population is limited by the nominal plasma density. The required number of macro particles inside the computational domain is a matter of trade-off between the time and accuracy. The higher the number of macro particles, the better the accuracy and longer the simulation time. In SPIS, we can only specify the average number of particles in a cell. This implies that if the ratio of cell volume (as mentioned before) is very large then there won't be enough particles inside the smallest cells, which are supposedly near to the high gradient regions. In other words, the numerical noise would be higher in such a scenario. On the other hand, a very small ratio (<1000) ensures sufficient number of particles in all cells. At the same time, keeping a very low ratio would raise the number of cells inside the domain resulting in longer convergence times. The effects of average number of PIC and ratio of cell volumes on simulation results are presented along with the test case results (chapters 8 and 9).

Another important feature of Gmsh is the possibility to create physical entities that override the geometrical entities. This enables a better user control over the meshing by proper orientation of mesh elements and also by grouping together the elements of different elementary entities having the same physical meaning. For e.g, in our case we can group all the outer boundaries of the simulation box as one physical entity. This facilitates the assignments of boundary conditions much easier rather than assigning to each side.

The size of the simulation box deserves utmost attention as it dictates the influence of boundary conditions on the simulation results. In our case, both Dirichlet and Neumann conditions are employed to validate its effects on the results. In case of Dirichlet boundary condition ($\Phi = 0$), the computational box has to be sufficiently large so as to ensure a minimal influence. The main advantage of Dirichlet is its easy implementation, but by forcing the boundary potential to zero significantly affects the potential derivative inside the

computational box, unless the walls are at a distance where the potential has decayed to near zero values. Since a larger simulation box augments the computational time, a minimum limiting distance has to be set for the outer walls. A theoretical criterion is that the walls should not be closer than a few λ_D so that the Debye shielding decreases the potential to low levels. On the other hand, using Neumann boundary conditions, it is not the potential but the normal derivative of the potential is set to zero. Such a condition wouldn't affect much the potential derivative inside the simulation box as before. Nevertheless, it would underestimate the potential values (as it forces the normal component to zero) on the outer wall boundaries if the distance to the wall is smaller.

7.3 SPIS-Num

This is the core numerical architecture of SPIS that empowers the modelling features required for simulating dynamic interactions. It is basically a plasma-spacecraft coupled system with an object oriented structure, enabling the integration of user defined plug-in classes to the already defined parent classes. The schematic view of the SPIS code structure is depicted in figure 7.3. The structure resembles a nested loop where by the top simulation level represents

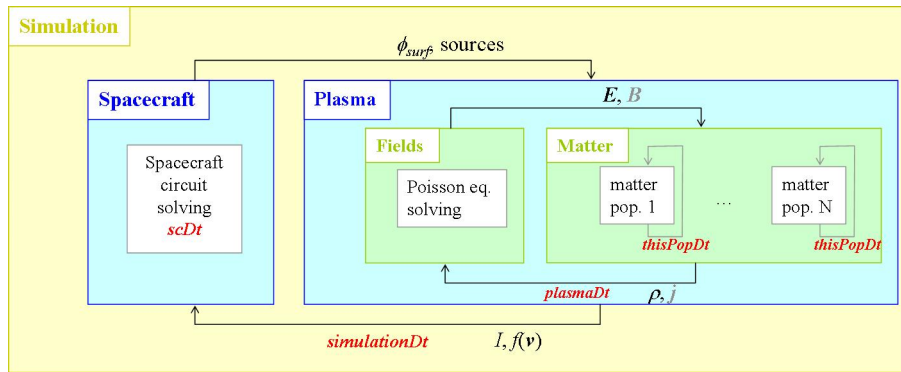


Figure 7.3: Numerical structure of SPIS code (*Roussel, et.al*^[6])

the plasma spacecraft coupling, while the plasma dynamics is defined by matter and field coupling at the next level. The integration time would be different for each level as well as various matter models depending on the constraints such as cell crossing time, plasma period etc. The time steps can be user defined or automatic, and applied recursively at each level.

In SPIS, currently the plasma is modelled as matter-field coupling but there is the possibility to implement a single magnetohydrodynamic (MHD) model. Two types of matter models are integrated in SPIS, the PIC model with a linear weighted charge distribution on nodes as explained before and a global Maxwell-Boltzman distribution. In this study, a PIC model is employed for the electron and ion distribution. The motion of each of the macro particles is traced with the following set of equations, along with the Poisson equation (4.6) mentioned in chapter 4 (*Engwall*^[3]):

$$M_i \frac{d\mathbf{v}_n}{dt} = Q_i (\mathbf{E} + \mathbf{v}_n \times \mathbf{B}) \quad (7.1)$$

$$\frac{d\mathbf{r}_n}{dt} = \mathbf{v}_n \quad (7.2)$$

where n represents the macro particle ($n = 1 \dots N_{macro}$), i the species (electrons/ions), M_i the mass of a macro particle (sum of all individual plasma particles making up the macro particle), Q_i the charge of a macro particle (sum of all individual particle charges in

a macro particle), \mathbf{r}_n and \mathbf{v}_n are the position and velocity vectors respectively. The total number of macro particles, N_{macro} , can be varied as a trade-off between required accuracy and computational time.

The above equations are integrated using a leap frog method, exact to the order two in dt . The resulting mathematical expressions can be found in chapter four of *Engwall*^[3]. An exact trajectory solver by analytical integration is also possible when \mathbf{B} is zero and \mathbf{E} is constant in each tetrahedral cell. Such constant \mathbf{E} is the approximate case when there are no imminent singularity sources like thin wires or thin surfaces in the structure that cannot be resolved by meshes due to the computational limitations.

In general, \mathbf{E} is considered as dynamical electrostatic field while \mathbf{B} is taken as user defined uniform value. The resulting Poisson equation for the potential is approximated using a finite element model on the unstructured tetrahedral mesh. The resulting linear system of equations is then solved by a conjugate gradient method. The boundary conditions can be chosen to be Dirichlet or Fourier (Robin condition: $\alpha\Phi + \frac{d\Phi}{dn} = value$ (here n represents the normal direction), where α and value can be implicitly defined with the option to mimic a $1/r$, $1/r^2$ or $1/r^n$ decay of potential towards the boundaries). Further features such as non-linear Poisson implementation of the conjugate solver, the analytical singularity extraction while dealing with thin wire and surfaces, volume interactions in modeling mater dynamics etc are explained in detail in *Roussel, et.al*^{[1],[6]}.

For spacecrafts, the movements of electrical charges are modeled by an equivalent circuit, consisting of mainly capacitors and resistors. The surface coating over the spacecraft is represented by a series of capacitors spread over the surface, with parallel resistors added to take into account the leakages through them. These are called continuous components and such an equivalent circuit is shown in figure 7.4.

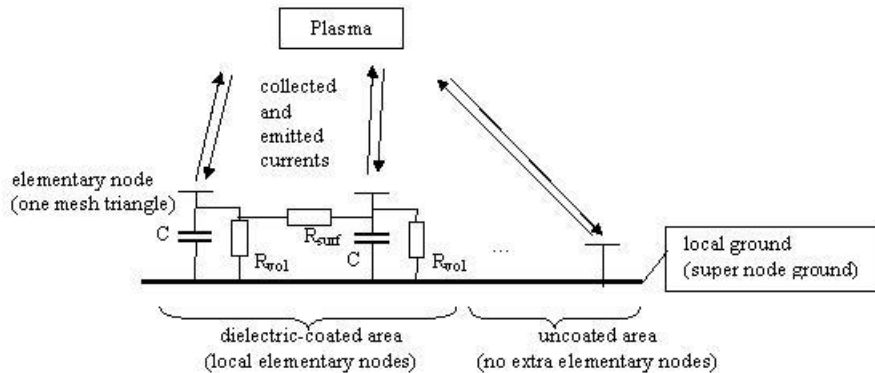


Figure 7.4: Spacecraft equivalent circuit with continuous components (*Roussel, et.al*^[6])

It is also feasible to include real electronic components, such as a decoupling resistor, an active bias etc, in the equivalent circuit. These are called discrete components and can be added between the subsystems referred as electric super nodes. The resulting circuit is depicted in figure 7.5.

The continuous components are generated automatically with coating capacitance (C) and resistance (R) values derived from the material properties. On the other hand, the discrete components are user defined in an ACII file (circuit.txt) with the values (C , R and V (voltage)) plugged in between the electric super nodes. The resulting linear matrix system describing the time evolution of potential takes the following form:

$$\frac{d\phi}{dt} = C^{-1}I \quad (7.3)$$

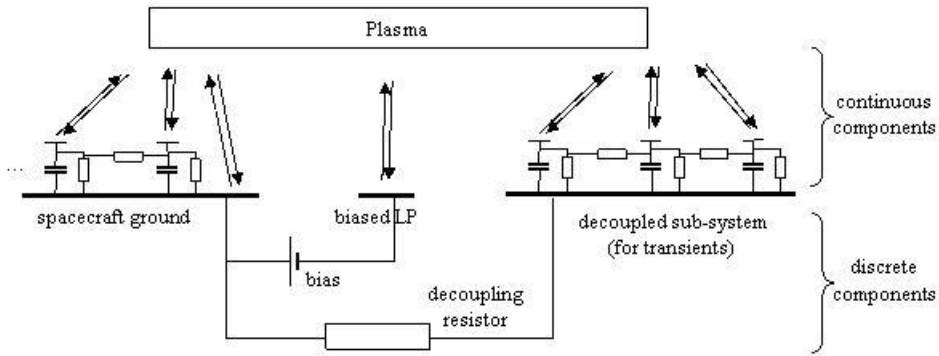


Figure 7.5: Spacecraft equivalent circuit with continuous and discrete components (Roussel, et.al^[6])

$$I = G\phi + I_{collected} - I_{emitted} \quad (7.4)$$

where I represents the current, C the capacitance matrix and G the conductivity matrix.

The explicit circuit solver presently implemented imposes a constraint on the time step that it shouldn't be smaller than the smallest eigen value of the matrix set. The main part of the spacecraft model deals with the modeling of material plasma interactions. The implemented interactions in the SPIS version, used here, are photo-emission, secondary emission from electron impact, secondary emission from proton impact and radiation induced conductivity (refer equation 5.4). The details of these are presented in Roussel, et.al^{[1],[6]}.

7.4 SPIS-UI

The main design motivation behind the development of an advanced user interface for SPIS has been to bring under one roof the user requirements of scientific and industrial spheres. The design is based on structured integration of independent tools, as modules on an open platform, with a central task manager controlling the actions on each module. A common data exchange bus facilitates the data exchange between modules as well as between the modules and common data structures. The schematic representation of SPIS-UI design is depicted in figure 7.6.

A detailed description of the SPIS-UI architecture is outside the scope of this work. The main aspects which are of interest are the simulation settings employed via UI during the pre-processing part and the post processing tasks. So in this section, instead of going further into the design, we will discuss the attributed settings and its relevance to the simulation scenario.

The CAD module is based on the open-source external tool Gmsh, with its own GUI for modeling the spacecraft geometry. It is executed as external standalone software as soon as the task manager calls the CAD definition module. Apart from geometry creation, Gmsh also performs the meshing of the computational domain. As per the order of tasks in the used version of SPIS, the meshing is done at a later stage, with Gmsh again called at that time. The creation of physical groups allows to group together geometrical entities possessing the same local parameters, which are scalar fields. This facilitates the easy implementation of boundary conditions as mentioned previously. We can add new entities using Gmsh GUI, but changes can only be carried out by editing the geometry file. The group managing can be done inside SPIS like this, if the geometry has been created by some other CAD software. Also it is possible to create geometry and define groups using Gmsh outside SPIS and then

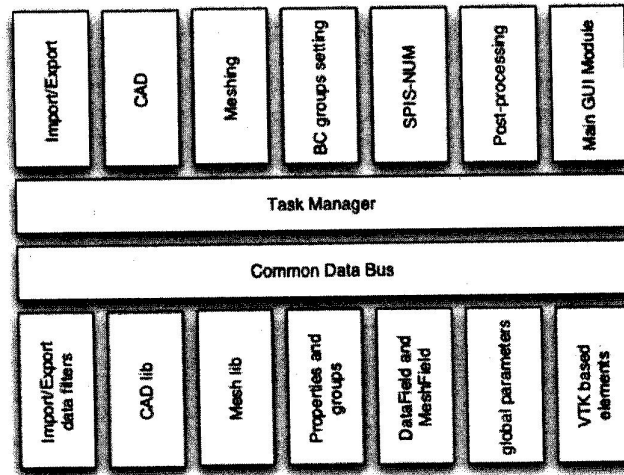


Figure 7.6: Top-level design of SPIS-UI (Roussel, et.al^[12])

opening the resulting structure in SPIS. The later approach is employed throughout in our simulations. In general, the user defines three physical groups in the CAD tool: spacecraft surface groups, external boundary groups and volume groups. After making all the required changes, the structure can finally be loaded into SPIS.

The next task in line is the setting up of boundary conditions, which corresponds to the definition of numerical and physical properties of local parameters, and attributing it to the different physical groups. The boundary conditions for each physical group are associated with the material, electric node and plasma properties. Assigning a typical condition to any of the groups would affect the properties of each of the elements constituting the group. There are two ways by which the user can define the properties, either by adding a new property according to the simulation requirement or by loading the pre-defined ones from the properties module and then editing it. Adding a new one in the source code is easier than through UI, but for a novice user, it is recommended to edit the pre-defined ones instead. The properties settings involve flags, directing the solvers about the type as well as localization of a boundary condition, that are all prone to errors at the hands of a not so experienced user so until a proper understanding of the code is attained it is better to go with editing the default values.

After loading the predefined properties, it can be edited using the properties editor. The material properties describe the physical characteristics of the used material. At present, only material models based on NASCAP database are implemented. In the material editor, we can choose the type of material and also include the emission (photo, secondary electron and/or secondary proton) as well as conductivity (volume, induced and/or surface) characteristics. One feature that requires considerable attention is the localization of assigned properties. If we are dealing with surfaces, then the localization (local) is indicated as 2 but for edges as in the case of thin wires it should be 1 (also 0 for nodes and 3 for volumes). In the present simulations, as we are not considering any emission interactions and are dealing with physical surface groups, all the emission flags can be turned off and localization be set to 2.

The electric properties refer to the internal charge balance of the spacecraft. There is only one electric node property, which is the choice of type of node (spacecraft ground, array ground, biased probe etc). In our case this is chosen such that the spacecraft is set to ground. Both the electric and material properties pertain only to the spacecraft physical group.

The plasma properties impute to the numerical setting of boundary and initial conditions

of the plasma numerical model and have to be defined for the whole computational domain. For plasma properties, there are three types that can be assigned to each of the physical groups namely plasma spacecraft, plasma boundary and plasma volume. In case of plasma on spacecraft, the default initialization is a Dirichlet potential on the surface nodes (local = 0) along with other attributes. This is an error in SPIS, as it includes some diffusion when mapped on surfaces, and to remedy this, potential has to be localized on the surface by setting the local to 2. The numerical value of the potential can be set according to simulation requirement. When dealing with thin wires, the wire is modeled as an edge so the local should be put to 1. The radius of the wire is specified via the edgeRadius option so that the thickness of the wire is not meshed. A thin wire plasma boundary condition, which can be loaded and edited, is also predefined in SPIS.

Dirichlet, Neumann and Fourier (mixed Dirichlet-Neumann) boundary conditions can be designated for plasma boundary, with the default set to Fourier. The Dirichlet condition is chosen by turning the BdDiriFlag to 1 and BdFourFlag to 0. A Neumann condition is already implemented as such. The localization should be done on the surfaces when employing the Dirichlet condition, while it has been defined on surfaces by default for Fourier and Neumann conditions. Different plasma boundary conditions, uniform as well as mixed, are tried out in the simulations to investigate its effects on final results.

There is only one plasma volume condition and it is used in its predefined form. Thus for volume groups and external boundary groups, there is only the plasma setting required. For spacecraft surface groups, along with plasma properties, material and electric node properties have to be defined. The interesting thing to point out here is that even though the solvers, at present, do not use the electric nodes, they have to be defined to run the simulation. Finally after defining the required boundary conditions, they are assigned to the concerned physical groups by calling the group editor task.

In the next step, the structure is meshed by calling Gmsh as external tool. We have so far assigned the boundary conditions to the physical group. But the solver needs values in the cells and nodes so solve the set of governing equations. This would require the physical groups to be converted to mesh groups first. This conversion would mark individually each mesh element according to their respective CAD groups. Now this has to be mapped on the entire mesh field to get a continuous field on the whole mesh. In SPIS, meshing, groups' conversion and mapping are linked by a dependence tree and these operations can be performed either individually or in group by clicking the field button, which will automatically call the three tasks in right order.

The final settings ascribe to the global parameters, which are concerned with the general behavior of the numerical solver, for e.g. simulation duration, magnetic field etc. A list of parameters with default values that can be edited are defined in the global parameters editor. They correspond to, though not in order, the settings for simulation control, plasma distribution, Poisson equation, magnetic (B) field, spacecraft, particle sources on spacecraft, interactions and outputs. We will not discuss here all the parameters related to the mentioned settings, but the necessary and important ones that have to be changed according to our present simulation requirements.

The most important parameters associated with simulation control are plasmaDt (time step for plasma dynamics) and duration (duration of the simulation). The time step can be set either manually or automatic. If the default value of zero is retained, then the time step is evaluated automatically so as to satisfy the stability criteria. It ensures that the particles don't cross more than a fraction of a cell within the time step and the condition is mathematically expressed as $dt < \frac{1}{\omega_{pe}}$ where ω_{pe} is the plasma frequency given by equation 3.3. The default option is chosen for our simulations. For duration, the time corresponding to $\frac{x_{SB}}{u}$ where u is the flow velocity of ions and x_{SB} the simulation box dimension in the direction of flow, is used. The magnitude of u depends on the ion-electron mass ratio (m_i/m_e) and corresponds to a value of 44 km/s for real mass ratio, for the case we want to simulate. All the simulations are done using this real mass ratio.

There is a slight disadvantage with SPIS that the user cannot control the mass ratio. The duration of simulation can be kept lower, for the same simulation box size, with a higher ion velocity. The increased ion velocity is not of a concern regarding the wake formation as long as the criterion for enhanced wake, as expressed in equation. 5.6, is satisfied. Lowering the mass ratio brings the ion velocity to higher values. On the other hand, if we can't manipulate the mass ratio to increase the velocity, keeping a lower duration would result in the ions not traversing the entire distance, x_{SB} . Two cases are simulated to check this effect and the results are presented in chapter 9.

The plasma distribution parameters define the type of distribution, temperature, density and velocity for electrons and ions. Two populations for each species can be taken into consideration, first population (incoming plasma particles) and second population (arising from photo and secondary emissions). In our simulations, the secondary population is omitted as the effect of photoelectron emission (with typical energy of about few eVs) is negligible due to the re-capturing of emitted electrons by the high positive spacecraft potential in the range 20-35V. Thus there won't be any appreciable built up of charge due to photo emission around the spacecraft. There are two types of particle distribution possible in SPIS, a global Maxwell-Boltzmann (GlobalMaxwellBoltzmannVolDistrib) and a PIC model (PICVolDistrib). The PIC model is employed for both ions and electrons in our simulations. Except for test cases (section 8) the boundary values for temperature and density are chosen to be consistent with the terrestrial magnetospheric environment, as obtained from Cluster and POLAR satellite observational data (*Engwall, et.al*^[8] and *Engwall*^[3]). These correspond to a temperature of 2 eV and a density of 0.20 cm^{-3} . The direction of flow is aligned with the positive X-axis, so only the velocity ($u = 44 \text{ km/s}$) along that axis (ionVx) is specified. The velocities in other directions are kept zero in the source distributions. Another important parameter concerned with the PIC model is the average number of particle in each cell (avPartNbPerCell). This number is of utmost relevance to the computational time as well as accuracy of the simulation and also it depends on the ratio of cell volume, as explained previously. The number is obtained by dividing the required number of macro particles by the total number of cells in the computational volume. The simulations for cubes (chapter 9) and cylinders (chapter 10) are done using 4 million macro particles. A couple of simulations in cube are done with a lesser number of macro particles and its effects on the results are also presented. For the boom case, the macro particles are reduced to 3 million because of the time limitation.

All the parameters controlling the Poisson equation conjugate gradient solver are kept unchanged except the flag (linearPoisson) for choosing the linear or nonlinear Poisson equation. The default value is set to 0 under the assumption of a Maxwellian distribution of ions/electrons. As we use a PIC model instead, for the distribution, the Poisson system is linear so the flag has to be set to 1. This is not inevitable because even if not changed, the system will automatically select the solver according to the species distribution.

The default magnetic field settings of zero magnitude in all directions are retained because in the magnetospheric regions with cold and tenuous plasma, field is typically very low (about 100 nT). Neglecting the magnetic field would cause the electron density in the wake to be under estimated but this is of not serious issue as the flow velocity is subsonic with respect to electrons.

The main settings for the spacecraft are the initial global potential (initPot) and the flag for spacecraft electric circuit integration (electricCircuitIntegrate). The initial potential has to be set according to simulation requirement. The flag, if set to 0, indicates that the potential on the spacecraft is constant. If set to 1 the potential floats, with the relative capacitances being derived from the material properties. A constant potential is applied for all the simulations.

The other parameters, for controlling the particle sources on spacecraft and interactions, are not of relevance in our present work as we are neither using any particle source such as an ion gun in our spacecraft nor dealing with any sort of interactions such as photoemission

or electron/proton secondary emissions. Also for controlling the outputs the default values can be kept as such.

So far, we have done with setting up all the material, plasma, electric and global parameters as per the simulation requirements. All these have been set through SPIS-UI, the data structure of it has to be converted to that of SPIS-NUM before calling the numerical solver. This conversion task build up the numerical model using the above defined parameters and the model is then solved according to the numerical procedures and mathematical expressions explained in section 7.3 and chapter 4.

On to the post processing part, the 2D plots can be obtained directly using the in-built basic viewer or exported in ASCII format for processing in other tools such as Matlab. All the 2D plots are extracted here using Matlab for simplicity. For obtaining 3D figures, a datafield conversion is required as the localization of data would be different for the computational grid and that for 3D interpolation. In computational grid, the data would be computed on the nodes but for 3D views, we need a continuous representation on cells with a linear interpolation. Such conversion are done using the datafield manager and saved as VTK (Visualization Tool Kit) data sets. It is then opened in Paraview to extract the output displays. We will not delve here much in to these visualization tools because the details regarding the use of VTK and Paraview are easily available on web as both are open source freely available software.

Finally, as a reference for the future users of SPIS, a step-by-step procedure to be followed in simulating a cylinder in plasma is given in Appendix A. An important point to note here is that it may not be the best setting for the case considered. Also experienced users may find faults in the employed settings as it is based on just 3.5 months of novice experience in the code. Nevertheless, it would serve some basic insights into the procedures for fresh users.

Chapter 8

Sphere Simulations

8.1 Introduction

In this section, the test cases simulated in *Roussel, et.al*^[5] have been redone to evaluate the results as well as to get some insights into the simulation settings. Two passive spheres (no particle emissions) in plasma flow have been simulated to verify the numerical accuracy of the code as well as the properties attribution and global parameter settings by the user. The basis for selecting a uniform conductive sphere rather than any complex shape is due to the fact that theoretically proved expressions exist for electron current collected by a uniform sphere at positive potential. One such expression is called Orbit Motion Limited (OML), formulated by Mott-Smith and Langmuir in 1926, that is valid for probes much smaller than the Debye length, and is as follows (*Roussel, et.al*^[5]):

$$I = 4\pi qn\sqrt{\frac{kT}{2\pi m}} \left(1 + \frac{q\Phi}{kT}\right) a^2 \quad (8.1)$$

where I is the collected current, q the particle charge ($q = -e$ for electrons), n the electron density, k the Boltzmann constant, m the electron mass, Φ the sphere potential, a the sphere radius and T the plasma temperature.

The collected electron current values obtained from simulations have been compared with that of OML for both the cases. Further investigations that have been done are to check the effect of boundary conditions (Dirichlet and Neumann) and the cell volume ratio (the largest to smallest cell volume in the computational domain) on the results.

8.2 Passive sphere of radius 0.25 m

A conductive sphere of 0.25 m radius immersed in non-flowing Maxwellian plasma is simulated. The general characteristics of the sphere and plasma are given in table 8.1.

| Parameters | Numerical values |
|------------------------------|------------------|
| Temperature (T) | 1 eV |
| Electron density (n) | 10 cm^{-3} |
| Debye length (λ_D) | 2.4 m |
| Potential (Φ) | 10.0 V |
| Sphere radius (r) | 0.25 m |
| Simulation box size | (10×10×10) m |

Table 8.1: General parameter settings for the simulation

Five simulations have been performed for this sphere, each with different settings for number of macro particles, cell sizes and outer boundary conditions. The simulation settings for each case are tabulated in table 8.2.

| Test cases | Outer boundary | Cell volume ratio | Macro particles | Average PIC |
|------------|----------------|-------------------|-----------------|-------------|
| Case 1 | Dirichlet | 27,000 | 300,000 | 60 |
| Case 2 | Dirichlet | 27,000 | 1,000,000 | 217 |
| Case 3 | Dirichlet | 3,375 | 300,000 | 14 |
| Case 4 | Dirichlet | 125 | 300,000 | 16 |
| Case 5 | Neumann | 125 | 500,000 | 26 |

Table 8.2: Simulation settings for various test scenarios

As mentioned previously, we have neglected the magnetic field in the simulations. This would impact on the result for larger simulation box sizes. If the simulation box size is larger than the electron gyro radius (30 m), some over estimation of electron densities in the wake may possibly occur. The electron current collected for each of the above cases are depicted in figure 8.1, along with the OML value. The first two cases show large numerical noise

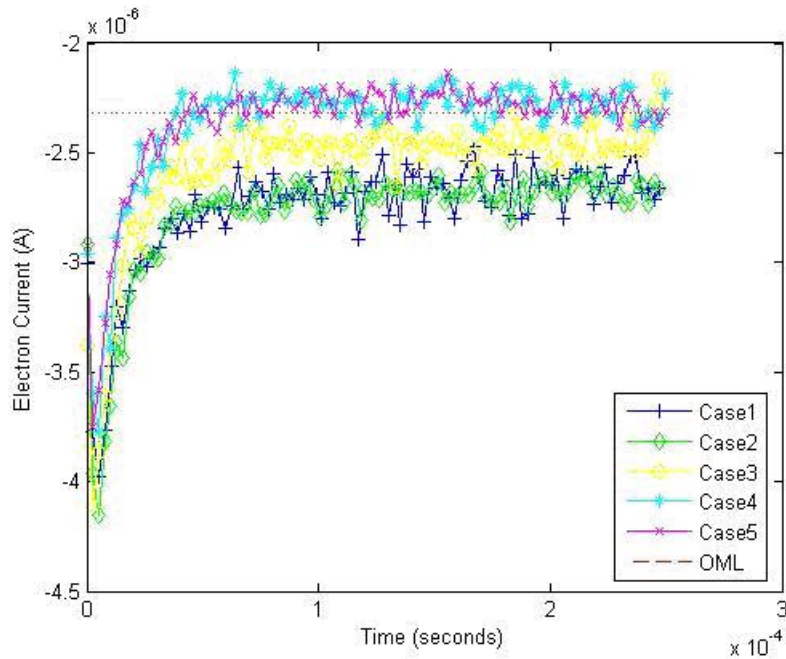


Figure 8.1: Electron current collected Vs Time

and also over estimates the electron current. This is due to the significant difference in cell sizes, employed while meshing the computational domain. The possibility to set only the average PIC in SPIS take away to a certain extent the advantages that can be achieved by unstructured meshing. Even though in case 2, a larger number of macro particles (or PIC) is used, apart from a reduction in the amplitude of fluctuations, the accuracy still lags. The effect of cell volume ratio is clearly evident as we move on to case 3. This is more accurate even though the noise is higher compared to case 2, which is due to the lesser number of PIC.

From the first three cases, it is clear that there should be an amicable balance between the cell sizes and the average PIC to ensure the best performance of an unstructured meshing scheme in SPIS. This is proven from the simulation results for cases 4 and 5, as both agree well with the OML value. Two different boundary types are employed for the outer boundaries, but the results are almost identical. This is quite obvious since we are using a very large simulation box, compared to the sphere radius, and also there is no flow condition prevailing in the whole domain.

The potential decay with the dimensionless radius as obtained from simulations is shown in figure 8.2. In this case, we are considering a Debye shielded sphere (since the sphere radius is less than the Debye length), the potential decay of which can be analytically expressed as:

$$\Phi(r) = \Phi \left(\frac{a}{r} \right) e^{\left(\frac{a-r}{\lambda_D} \right)} \quad (8.2)$$

where r is the radial distance from the sphere. This is also included in the plot as it gives a good estimate regarding the accuracy of the simulation results. The potential field for a sphere with the same potential in vacuum conditions is also plotted. If the sphere is assumed to be in vacuum, then the potential decay with the radial distance can be approximated as (Engwall^[3]):

$$\Phi(r) = \Phi \frac{a}{r} \quad (8.3)$$

The plot verifies that the SPIS agrees appreciably with the analytical models. A more

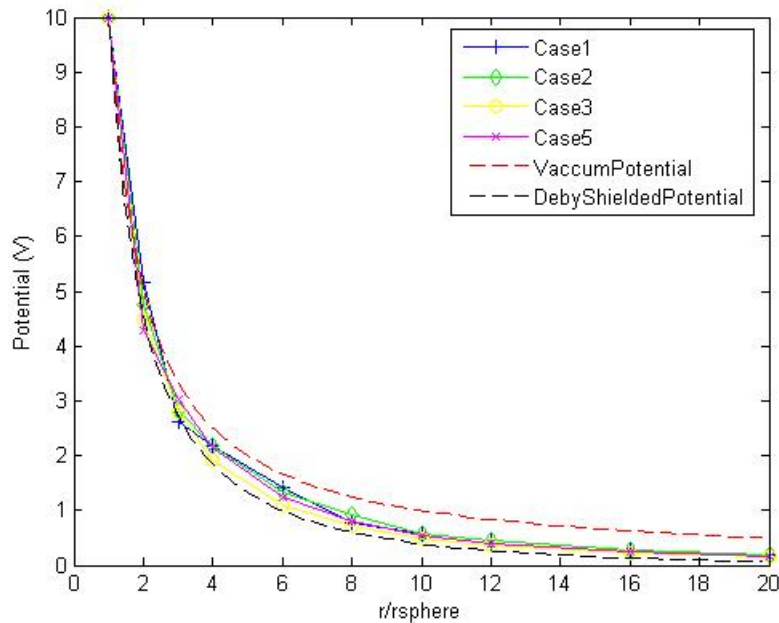


Figure 8.2: Potential Vs Dimensionless radius

qualitative representation of the potential as well as electron density are shown in figures 8.3 and 8.4.

In figures 8.4, the feature which deserves attention is the non-symmetric electron density structure around the sphere. Since we are employing a non-flow condition with a uniform sphere, the actual case should then produce a symmetric decay. This discrepancy, to a certain extent, is due to the non-uniform meshing around the sphere. Hence at this stage,

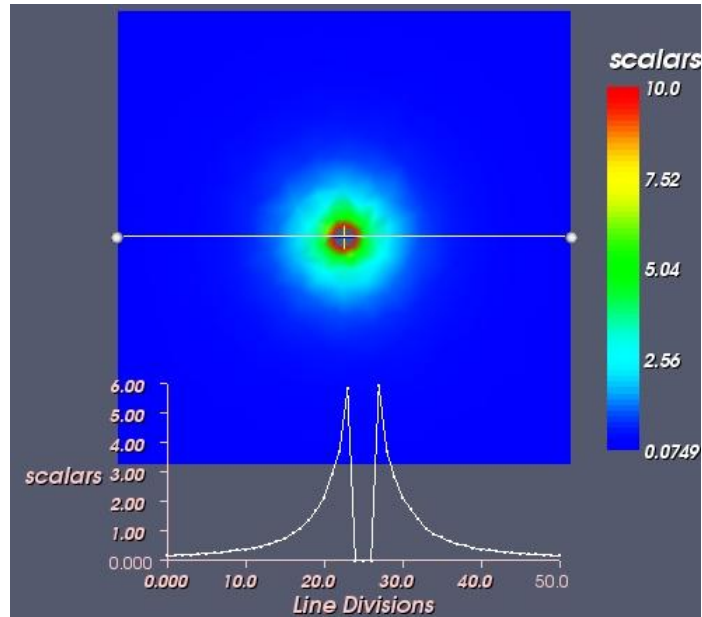


Figure 8.3: Potential decay from the sphere (Grid points in XY plane)

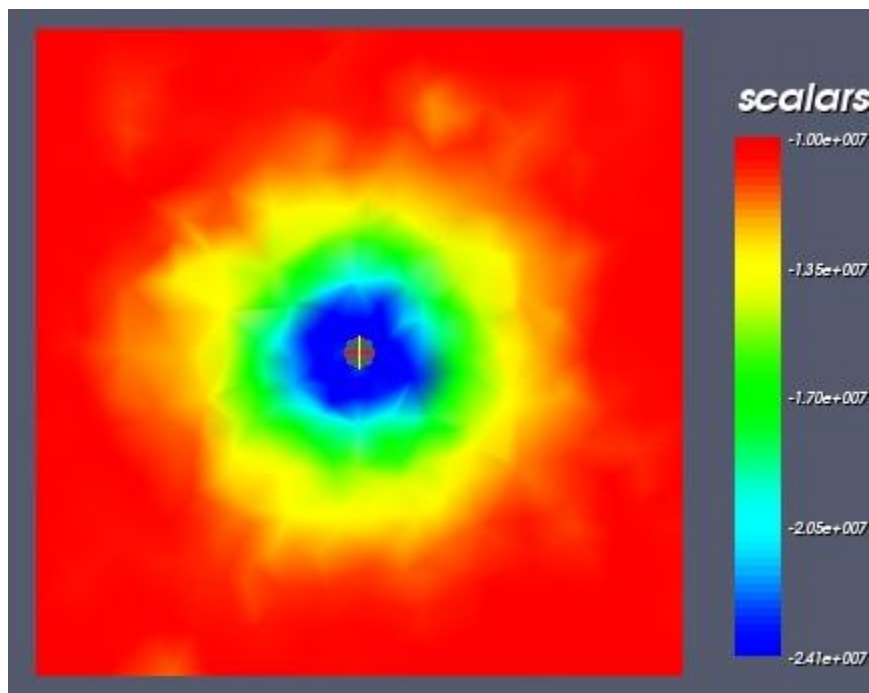


Figure 8.4: Electron density (Grid points in XY plane)

it is realized that a clever approach to avoid this disparity as well as to extract a better result would be to employ a block meshing (as explained before) around the structure. This scheme is used for the simulations with cube and cylinder (chapters 9 and 10).

8.3 Passive sphere of radius 1 m

In this a sphere of radius 1 m in higher electron density plasma is simulated so as to check the modelling ability of SPIS when the Debye length becomes comparable to the sphere radius. The simulation parameters are shown in table 8.3.

| Parameters | Numerical values |
|------------------------------|----------------------|
| Temperature (T) | 1.0 eV |
| Electron density (n) | 55 cm^{-3} |
| Debye length (λ_D) | 1.0 m |
| Potential (Φ) | 25.0 V |
| Sphere radius (r) | 1.0 m |
| Simulation box size | (40×40×40) m |
| Number of macro particles | ≈300,000 |
| PIC | 14 |

Table 8.3: Parameter settings for the simulation

The simulation is performed with approximately 22000 tetrahedrons and 300000 macro particles, employing Dirichlet conditions at the boundary. The results show good agreement with the OML model as depicted in figure 8.5 below. A slight tendency to stay below the OML result may possibly be discerned, which is not strange given that we are clearly outside the strict domain of validity of OML in this case as we have sphere radius as big as the Debye length.

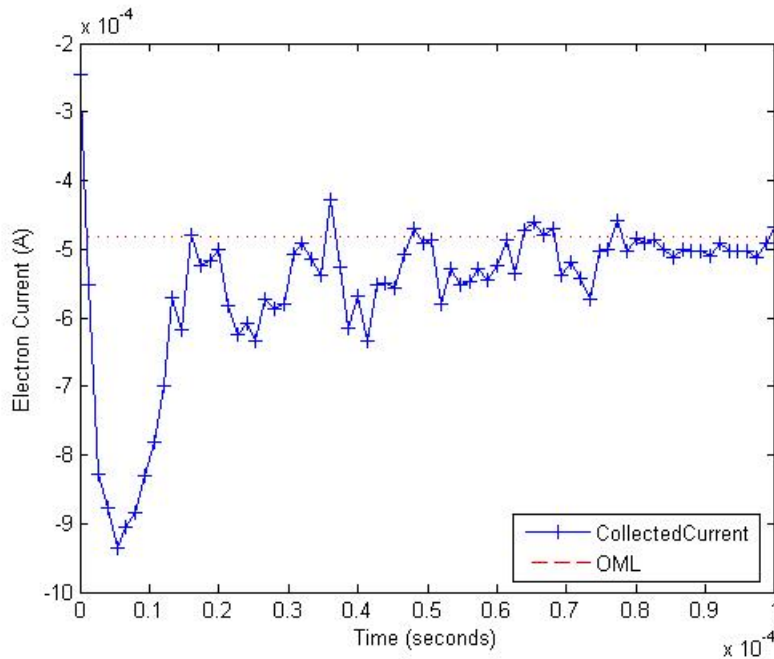


Figure 8.5: Collected electron current Vs time

Chapter 9

Cube Simulations

9.1 Introduction

In *Engwall*^[3], simulations of Cluster body without booms were performed by approximating the real cylindrical body with a cube and using similar software called PicUp3D. A cube was used for ease of modelling but then, instead of the real spacecraft potential, an effective potential had to be employed to take into account the exaggerative size of the satellite (made necessary by the finite resolution of the uniform rectangular grid in PicUp3D). In this section, the same simulations but done in SPIS are presented. It is comparatively simple to model a real spacecraft body (chapter 10) in SPIS, but these simulations are done before that to compare the results. Moreover, in order to speed up the simulations, an artificial mass ratio was used in *Engwall*^[3]. To verify the influence of such an approach in SPIS is another objective behind the re-computations. The simulation settings employed are outlined in table 9.1. The same cube size and effective potential of 16 V (representing

| Parameters | Numerical values |
|------------------------------|------------------|
| Temperature (T) | 2.0 eV |
| Electron density (n) | 0.20 cm^{-3} |
| Debye length (λ_D) | 24 m |
| Potential (Φ) | 16.0 V |
| Cube size | (4×4×4) m |

Table 9.1: Simulation parameters

the real spacecraft potential of 35 V), as used in PicUp3D simulations, are kept here also. First we discuss the artificial mass ratio effects and then go to the real simulations done, each with different boundary combinations.

9.2 Mass ratio

As explained in chapter 7, using artificial (or non-real) mass ratios we can manipulate the plasma flow velocity, thereby increasing or decreasing the simulation time. A higher velocity can be desirable as it would considerably reduce the total simulation time especially when large simulation boxes are used, though at least part of this gain may be lost by an increased need for time resolution. More important, a simple code moving the ions and electrons using the same time step would spend a disproportionate amount of resources on calculating ion motion at electron time resolution, without any gain in accuracy whatsoever: with an artificial mass ratio, the difference in time scales is decreased, and the waste of computer

time goes down. However, such an explicit manipulation would have to satisfy an implicit constraint. For a particular species, say ions or electrons, only the charge density varies depending on the flow condition as well as the spatial distribution of the species, but the charge remains constant. From the expression for Lorentz force (equation 4.4), we can infer that the charge is proportional to the velocity and mass of the species. So, in computations, any increase (explicit or implicit) in mass has to be compensated by a corresponding decrement in velocity and vice versa. Otherwise, the charge would increase (or decrease), which physically means a different species, resulting in a smaller (or larger) spatial density of species (equation 4.2) than the real situation.

In SPIS, we can only change the velocity of the species but there is no explicit possibility for changing the mass. The main reason for this is that there is no need: SPIS uses different time scales for integration of electron and ion motion, and hence there is no need for an artificial mass ratio. Nevertheless here two simulations are performed, with ion flow velocities of 44 km/s (corresponds to the real mass ratio) and 190 km/s (corresponds to a mass ratio of 100) respectively. Since we now are concerned more with the qualitative aspects of the results, a very small simulation box ($55 \times 30 \times 30$ m) is used for both computations. The results shown thus corresponds roughly to replacing the proton flow by a flow of oxygen ions at real speed, as a change of speed by a factor of 4.3 without a change of mass amounts to changing the drift kinetic energy by a factor of 18.6, not too far from the oxygen to proton mass ratio of 16.

From the plasma conditions, we expect an ion wake behind the structure as well a shock like ion region at the front due to the positive potential on the spacecraft. The ion densities obtained are shown in figure 9.1. We can see that the wake width now is set by the spacecraft geometry rather than by the potential field from the spacecraft, as expected for an ion flow kinetic energy higher than the spacecraft potential. This kind of narrow wake is representative of e.g. solar wind conditions (*Eriksson, et.al*^[10]).

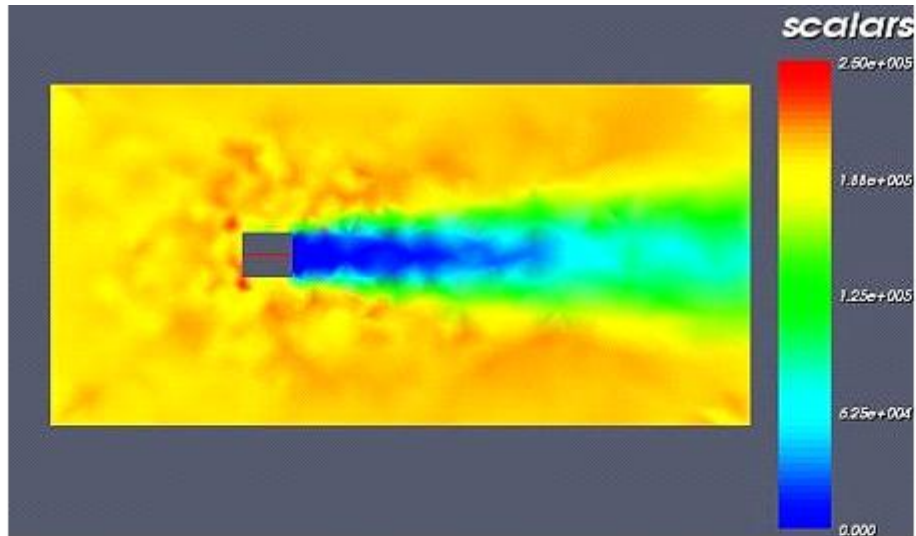
As there is no explicit way for changing the mass ratio in SPIS-UI, we can't blindly increase the ion velocity to reduce the simulation time, as is evident in a comparison of figures 9.1.a and 9.1.b. Unless the mass ratio is changed accordingly, a reduced simulation time would result in ions attaining a higher charge than the real value. Such a higher charge would reduce the spatial density of the species as evident in the under developed wake structure in figure 9.1.a. Hence it is decided at this stage to use the flow velocity (44 km/s) pertaining to real mass ratio for all further SPIS simulations.

9.3 Real simulations

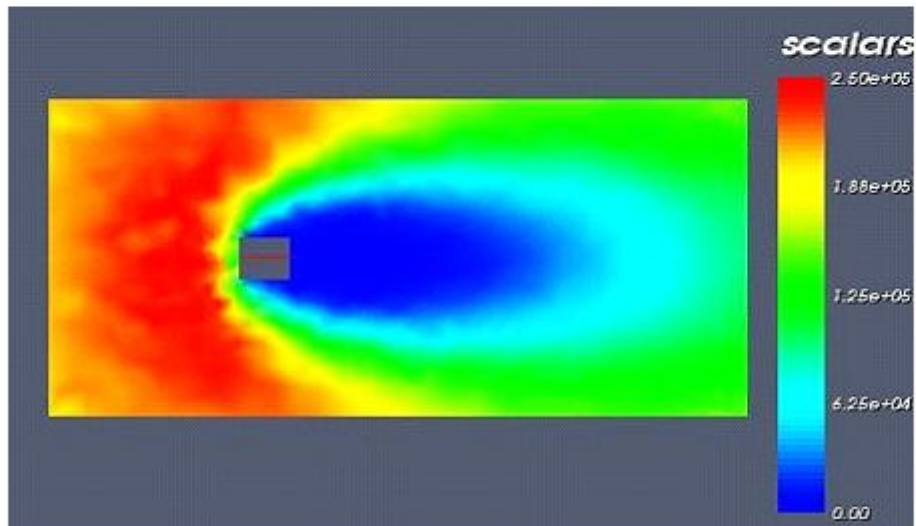
Two simulations are performed to verify the accuracy of results (especially the usage of an effective potential) and the influence of different boundary conditions. However, to ensure minimum influence of the boundary conditions on the results, a very large simulation box size ($250 \times 150 \times 150$ m) is chosen such that the walls at the upstream as well as sides are at a distance of $3\lambda_D$ and in the downstream at about $7\lambda_D$ from the cube. Also, such a large box would make it possible to make measurements at points, which correspond to the boom positions if it would have been included. If the Cluster EFW booms (44 m in length) are attached, walls of the chosen box would then be at least $1\lambda_D$ from the boom ends.

More than 3 millions macro particles are used in both the simulations. For first case, a Dirichlet boundary condition on the upstream end and Neumann elsewhere is used. The second case is simulated with Dirichlet boundaries everywhere. The ion wake structure behind the cube, as obtained for the first case is shown in figure 9.2. The second simulation case is not shown as it is almost identical since we have used a very large computational box and thus nullifying the influence of boundary conditions on the results.

The ion wake behind the positive cube is clear from figure 9.2 and the wake size matches with the results presented in *Engwall*^[3] and *Engwall, et.al*^[8]. The presence of such an ion



(a): Ion density for flow velocity of 190 km/s (Grid points in XY plane)



(b): Ion density for flow velocity of 44 km/s (Grid points in XY plane)

Figure 9.1: Ion density around the cube for two different flow velocities

wake would affect the electric field measurements significantly. A measurement boom in the downstream points would sense a lower potential if it lies inside the wake. Of course, the inclusion on booms would have changed the complete wake structure. Also the size of the wake would grow bigger for higher spacecraft potentials.

In order to make a quantitative comparison between SPIS and PicUp3D results, we need to look into the potential field. This is depicted in figure 9.3.

From figure 9.3, we can see that the potential decay around the cube gives almost spherical equipotential down to around 1 V. The presence of wake is confirmed by the negative potential behind the cube, with the minimum value reaching at -0.24 V. The corresponding

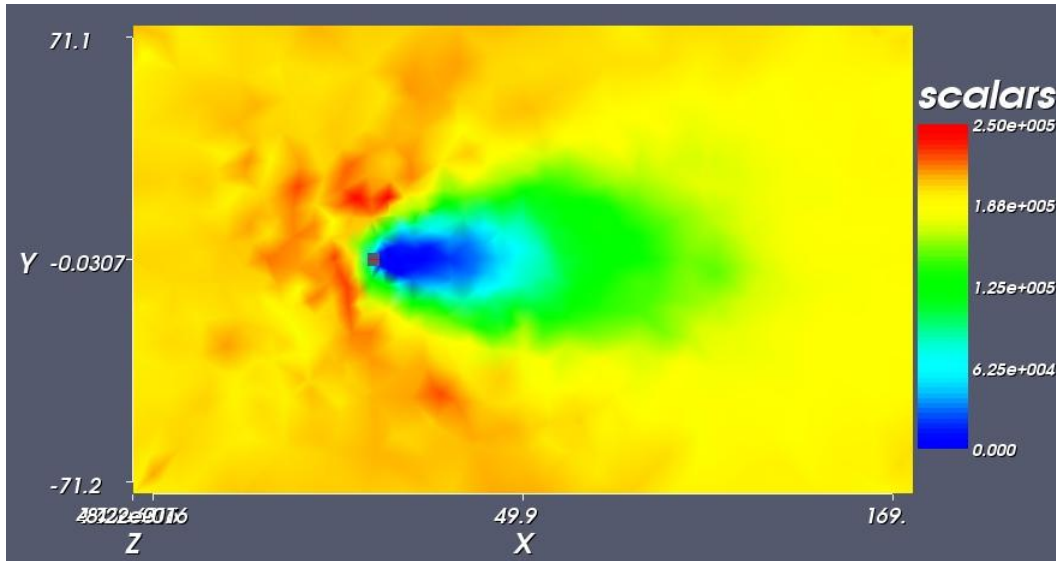


Figure 9.2: Ion density structure in XY plane

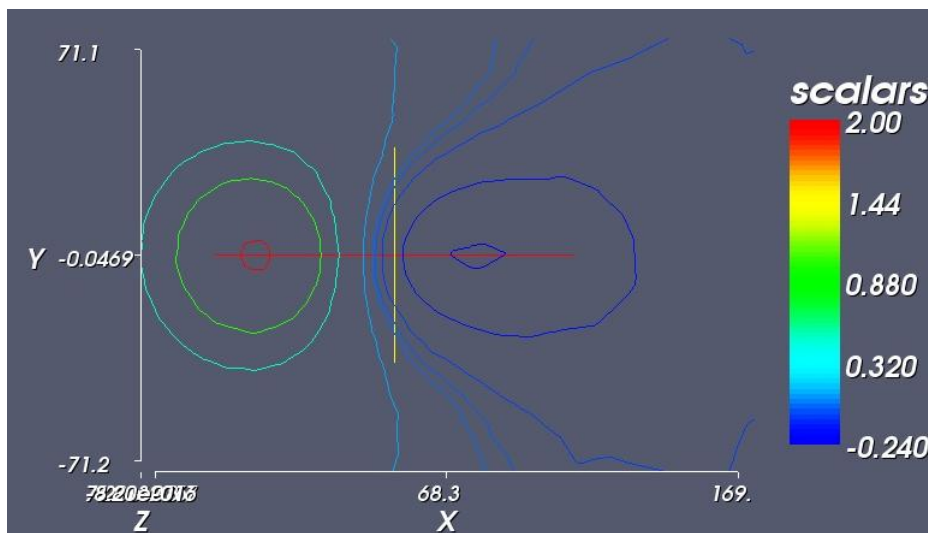


Figure 9.3: Potential obtained in the XY plane with a minimum value of -0.24 V (The equipotential contours are drawn for -0.24, -0.15, -0.05, -0.01, 0.01, 0.1, 0.5, 1 and 10 V)

minimum potential in the wake from PicUp3D in *Engwall*^[3] and *Engwall, et.al*^[8] shows a value of -0.3V. This slight mismatch could be due to the difference in grid schemes used in the solvers. However at this stage, without further analysis of the results, it is not possible to comment which code is better.

A more appreciable way to analyse the results would be to compare with that of measurements made by EFW instrument on Cluster. In *Engwall*^[3] (figure 18.b), the potential difference between two ends of the boom, made during one spin period (4 s) of the satellite, is shown. The plasma parameters used in this simulation characterises the real plasma environment at the spacecraft location when the measurements were obtained. The potential difference as obtained in our simulation is shown in figure 9.4. The simulation results show

a maximum potential difference of 406 mV, while the measurements give a value of around 480 mV. In this case PicUp3D results show a closer agreement with the maximum difference around 520 mV. However, we should note that the plasma density and temperature at the time of the observation are not well known at all, so that the PicUp3D result compares a little better to the data than do the SPIS result actually says nothing about the performance of the codes. What is important is that they agree reasonably well, within about 25 percent, and that they both produce signatures similar to data. Before drawing up a final conclusion we should check the efficiency of our chosen cube model in representing potentials especially at larger distances (which is the case when booms are included) from the real cylindrical spacecraft body.

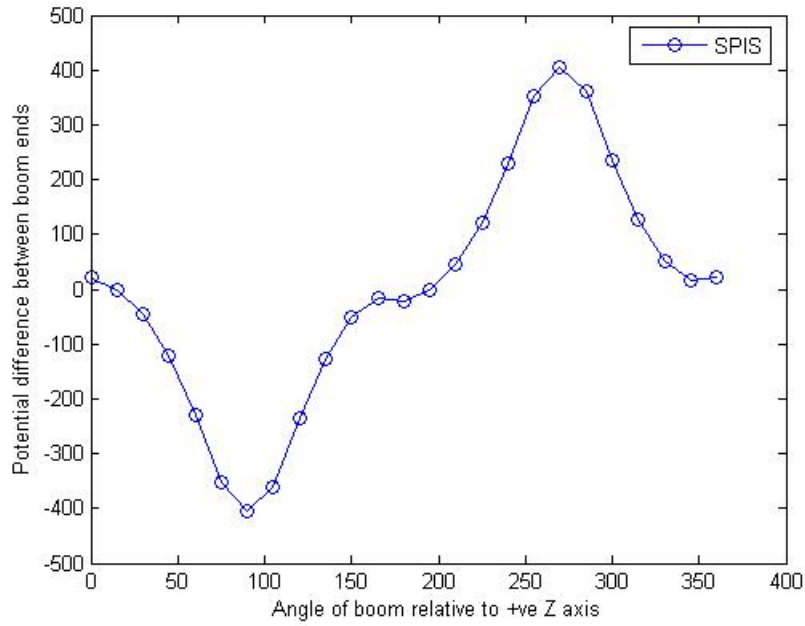


Figure 9.4: Potential difference between the probes at different flow angles

The effective potential of the real spacecraft body can be calculated by comparing it with a suitable analytical model. An appropriate choice would be the potential distribution around a Debye shielded uniform sphere, as given by equation 8.2. However such a model wouldn't completely imitate the present case since a Debye shielded model is based up on a linearization of the potential. It is accurate for potentials much below $\frac{kT_e}{q_e}$, which corresponds to 2 V as per the simulated plasma characteristics. Since our potential is much higher (35 V) than this, some differences do occur between the model and simulations. In order to find the sphere size which can effectively approximate the cylindrical spacecraft, we equate the surface areas of both bodies.

$$4\pi r_s^2 = 2\pi r_c^2 + 2\pi r_c h \quad (9.1)$$

where r_s is the equivalent sphere radius, r_c and h the radius and height respectively of the real cylindrical spacecraft. Putting the real dimensions ($r_c = 1.45m$ and $h = 1.5m$), we get a sphere radius of 1.46 m. The potential distribution obtained from the simulation is plotted together with this equivalent Debye shielded potential in figure 9.5. Also shown is the potential decay if the same sphere would have been placed in vacuum.

From figure 9.5, we can see that SPIS agrees remarkably well with the Debye shielded model. Another conclusion that can be drawn is that an effective potential model approach,

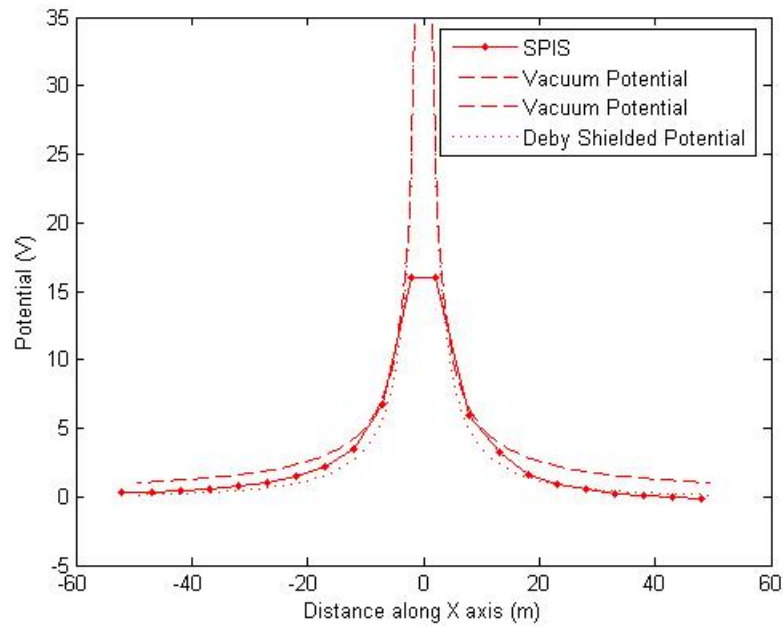


Figure 9.5: Potential from simulation plotted with analytical potential distributions around a sphere

as done here, is quite accurate in representing the real spacecraft geometry. This is very convenient in the sense that by using a suitable model with a simple shape, we could get rid of the modelling difficulties associated with complex geometries. Closer to the body, the approximation with an effective potential agrees appreciably with the analytical vacuum model. But as we go further away from the cube, the approximation degrades and the simulation results goes to zero potential faster than the vacuum model. This is because in real case, the negative wake attracts ions into the wake neutralizing the charge as we go away from the source.

Referring figure 9.4, we can conclude on the basis of figure 9.5 that the discrepancy in potential when compared to the observed data is not due to an effective potential approach. One reason for this disparity has already been mentioned there. Another possible cause would be the large mesh lengths (4 m: same as used with PicUp3D in *Engwall*^[3]) used in this simulation. At least within a Debye length from the source, the distance dependency of potential is very high. So the absence of a desirably small cell size near the source would have contributed to this difference when interpolated at boom end locations. Anyway, at this stage, this comment would rather be hypothetical but we could deduce a better conclusion regarding this in the next chapter, where the real spacecraft geometry is simulated with relatively smaller mesh lengths near the source.

Chapter 10

Cylinder Simulations

10.1 Introduction

In this chapter, the real geometry of Cluster spacecrafts without booms is simulated to investigate the wake formation. The spacecraft body has a cylindrical dimension of height 1.5 m and diameter 2.9 m. By using the real dimensions, the use of an effective potential is no longer needed and we can go on with the real spacecraft potential of 35 V. So a comparison could also be made regarding the accuracy in using the effective potentials. Except the potential, all other plasma settings are put the same as in cube simulations (chapter 9). The simulations parameters used are given in table 10.1.

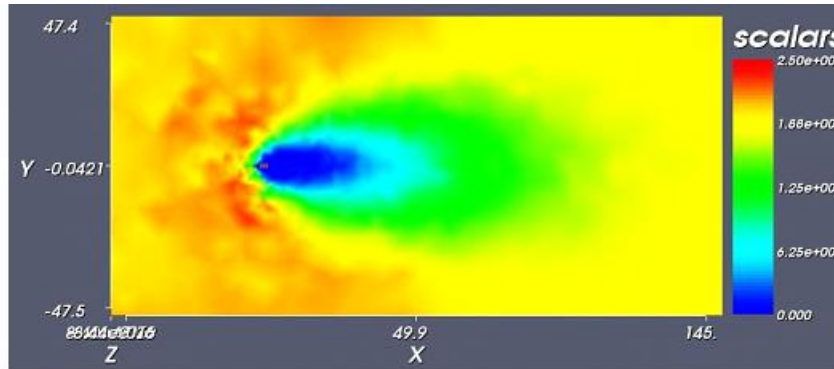
| Parameters | Numerical values |
|------------------------------|--------------------------|
| Temperature (T) | 2.0 eV |
| Electron density (n) | 0.20 cm^{-3} |
| Debye length (λ_D) | 24 m |
| Potential (Φ) | 35.0 V |
| Cylinder size | (1.5 h \times 2.9 d) m |

Table 10.1: Simulation parameters

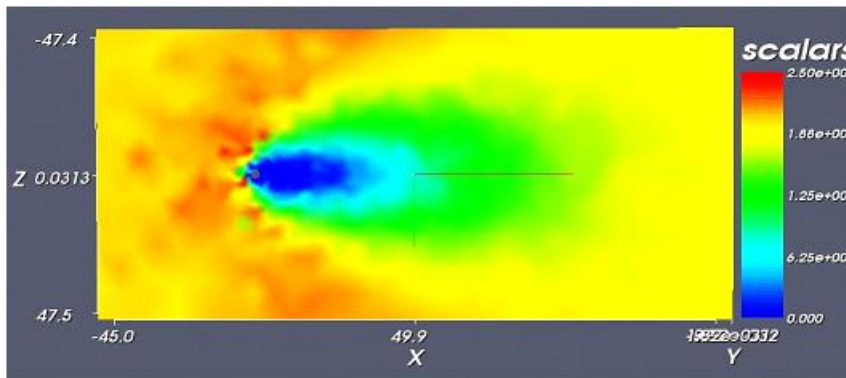
10.2 Simulations

Due to the time limitations, it is decided to use a smaller computational box since the real spacecraft's body dimensions are lesser than that of the cube. The present simulations are done with a box size of $200 \times 100 \times 100$ m. A conclusion deduced from the previous simulations is that by using a very large computational box ($3\lambda_D$ in the upstream as well as sides and $7\lambda_D$ in the downstream direction), the influence of boundary conditions on the wake structure is negligible. For the present case, it is reduced to $2\lambda_D$ in the upstream and sides, and $6\lambda_D$ in the downstream. This would, to a little extent, affect the potential development on the boundaries closer to the spacecraft body (cylinder), but is acceptable since we are more interested in the wake structure downstream. Also to minimize this influence, a Neumann boundary condition is chosen as it provides some flexibility to the boundary potential. So it is decided to use a hybrid boundary condition (Dirchlet at the flow entrance side of the box and Neumann elsewhere) for further simulations in this as well as in the next chapter. For better accuracy, the number of particles is increased to 4 millions, which corresponds to 122 PIC for the chosen box size and mesh characteristics. The flow velocity is kept at 44 km/s,

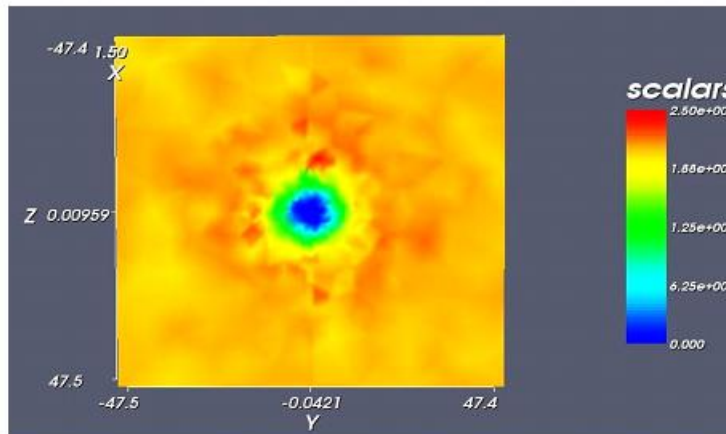
maintaining the real mass ratio. The simulation results obtained for ion density and the potential decay are depicted in figures 10.1 and 10.2.



(a): Ion density in XY plane (Grid points in m)



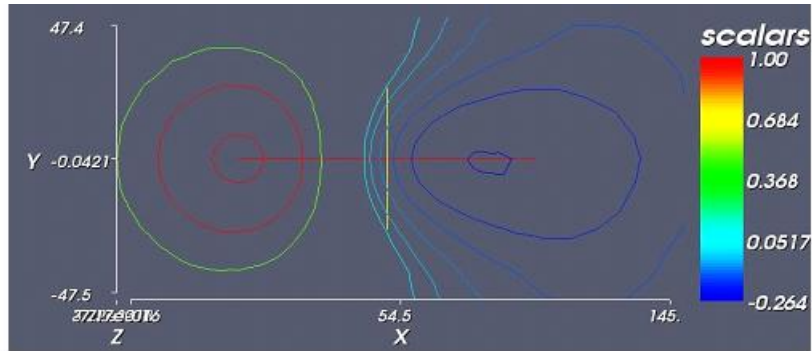
(b): Ion density in XZ plane (Grid points in m)



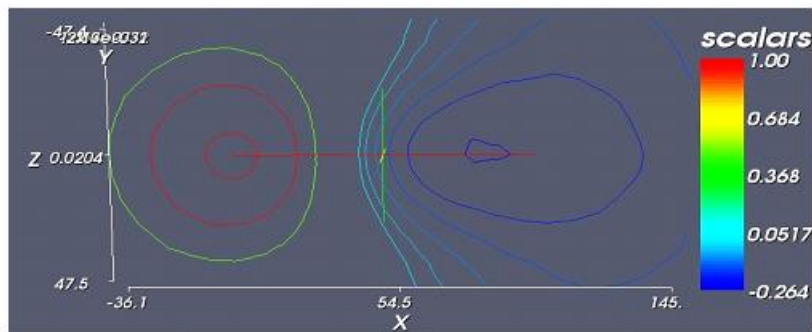
(c): Ion density in YZ plane (Grid points in m)

Figure 10.1: Ion density around the cylinder in various planes

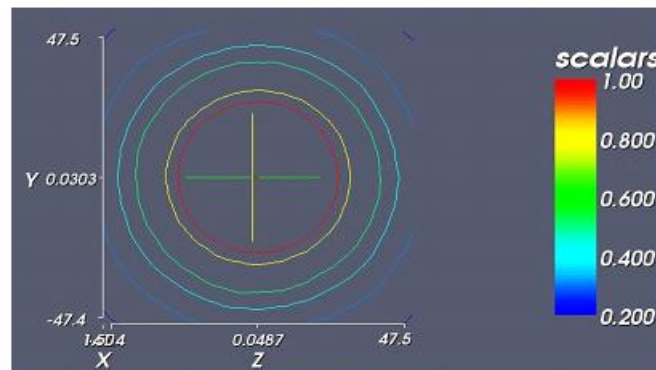
The results shown in figures 10.1 and 10.2 verify the presence of an ion wake that could significantly alter the measurement of EFW instrument. Considering the worst case scenario, if the booms are included and are aligned with the flow so that one boom is completely



(a): Potential in XY plane with a minimum value of -0.26 V (The equipotential contours are drawn for $-0.26, -0.2, -0.15, -0.1, -0.05, -0.01, 0.5, 1$ and 5 V)



(b): Potential in XZ plane with a minimum value of -0.26 V (The equipotential contours are drawn for $-0.26, -0.2, -0.15, -0.1, -0.05, -0.01, 0.5, 1$ and 5 V)



(c): Potential in YZ plane ($X=0.05$ m from the spacecraft) with a minimum value of 0.2 V (The equipotential contours are drawn for $0.2, 0.3, 0.4, 0.5, 0.8$ and 1 V)

Figure 10.2: Plasma potential around the cylinder in various planes

engulfed in the wake of the body as well as the boom on the other side, the location where the boom ends in the downstream direction corresponds to a potential in between -0.01 and -0.05 V, according to figures 10.2.a and b. However this is not the realistic case because in addition to the body the boom on the upstream end also contributes to the wake, enlarging it further and hence reducing the potential at downstream boom end to higher negative values. An accurate estimation is possible only by modeling a full spacecraft, including booms, but

it is not done in the present work due to the limited time. Nevertheless, we can get a clear picture by comparative interpolation of the separate analyses of body and booms (chapter 11). Also the plasma density and temperature influences the wake structure, thereby putting up a different scenario at different locations along the Cluster orbit. Moreover an increase or decrease in the satellite potential can vary the wake, making it bigger for increasing potential and vice versa.

The results agree appreciably with that obtained when an effective potential surface (4 m cube of 16 V) was used and also the wake size matches with the PicUp3D results, presented in *Engwall*^[3] and *Engwall, et.al*^[8]. However, the minimum potential differs by about 24 percent from the PicUp3D (-0.34 V) simulations. Again, this doesn't give an insight into the performance of both codes unless further analyses of the results are made with respect to theoretical models. So, as done with cubes, the simulation results are compared with that of potential distribution around a Debye shielded uniform sphere (with the same surface area as that of the cylinder). It is shown in figure 10.3, along with that of an effective potential surface (chapter 9) and vacuum potential distribution.

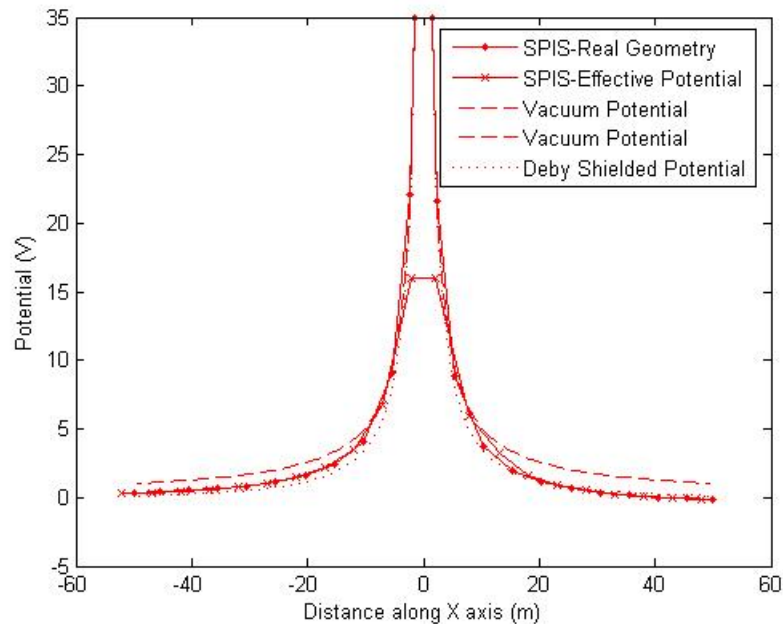


Figure 10.3: Potentials from simulations plotted with analytical potential distributions around a sphere

In figure 10.3, both SPIS simulations show appreciable agreement among themselves as well as with the Debye shielded model. Hence it reinstates the representative applicability of an effective potential approach in order to simplify the modeling complexity, especially when dealing with tools having limited modeling capabilities (such as PicUp3D). A little shift from the Debye shielded model, nearer to the source, is evident in the plot but is expected since the potential of the spacecraft is very high (35 V).

An accuracy check-up of obtained results can be made by comparing it with the observational data from EFW instrument onboard Cluster satellite, as given in *Engwall*^[3]. The potential difference between the probes for one full rotation of the satellite, as obtained from simulations, is shown in figure 10.4.

Figure 10.4 shows a maximum potential difference of about 500 mV, which astoundingly

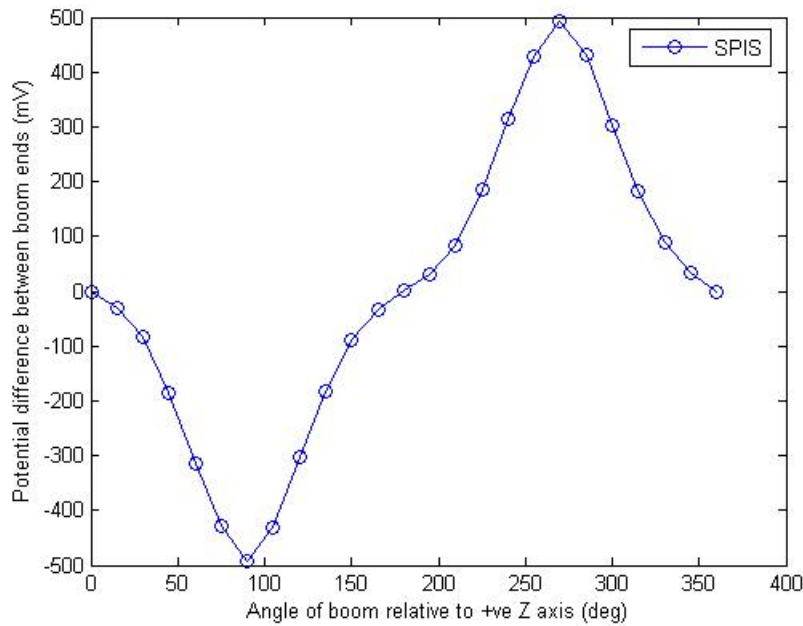


Figure 10.4: Potential difference between the probes at different flow angles

agrees with the instrument data. Anyhow, some disparity with observation may do occur due to the reasons explained in the previous chapter. The above plot supports our previous conclusion regarding the mesh dependency of the potential. By using an effective potential cube, we obtain a maximum potential difference of 406 mV, a less appreciable result. This is due to the larger mesh lengths (smallest grid size of 4 m) used. For cylinder simulations a minimum length of 1 m is used and it is then able to more accurately resolve the potentials at boom lengths from the cylinder. So the disparity between the simulation and observed data, in our cube simulations, would be predominantly due to mesh characteristics rather than to the obscure plasma characteristics at the time of observation. If it would have been due to the plasma properties, a difference of similar magnitude would have been reflected in simulations of real spacecraft geometry as well.

Regarding the influence of mesh size, the stringent distance dependency of the potential is depicted in figure 10.5.

In figure 10.5, it is clear that large potential gradients are present for a distance of about 15 m from the cylinder and it gradually reduces to nearly zero at about 50 m from the cylinder. Thereafter a relatively large mesh size wouldn't negatively influence the results. So for an accurate computation, it would then be appropriate to provide very fine grids within at least 15 m from the cylinder. A good proof of this is also evident in figure 10.5. The potential plot is drawn with a resolution of 1 m and even for a distance of less than 1m from the cylinder the potential has dropped to 29 V from 35 V.

The SPIS computations can be made more accurate by decreasing the mesh size towards the spacecraft. Obviously this would increase the computational time. However, such an approach is not possible in PicUp3D as it supports only uniform meshing scheme. So any decrease in the mesh size would considerably increase the total number of elements in the computational box. Also due to this structured mesh scheme, it is not possible to model complicated shapes in PicUp3D. There lie the main advantages of SPIS, where we could model any shape as well as provide grid sizes according to the requirement, with a com-

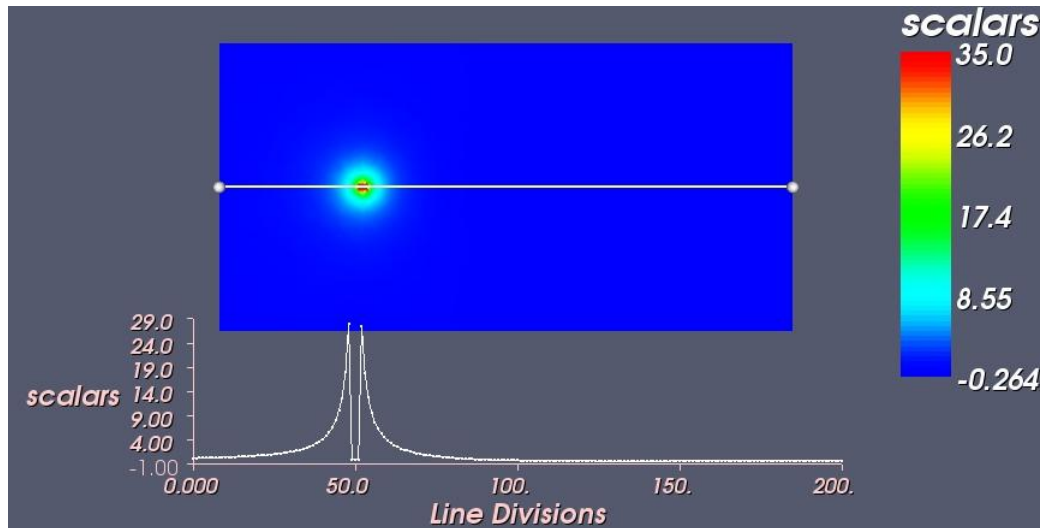


Figure 10.5: Potential decay along the X axis (distance in m)

paratively small increase in the number of elements. This would in turn facilitate shorter computational times especially when the domain is very large.

Chapter 11

Boom Simulations

11.1 Introduction

In this chapter, the results obtained from simulating the booms of the satellite are presented. The presence of the booms significantly affects the wake structure, from that presented in the previous chapters, implying a much lower potential due to larger wake. In Cluster satellites the EFW instrument probes are separated by 88 m with wire booms of diameter 2.2 mm. Also the probes are located 3 m out from the end of the boom, which has the same potential as that of spacecraft. Obviously, the wake from the booms would then influence the measurements made by the probes.

Some approximations are done in order to simplify the modeling tasks as well as to meet the time constraints. In the SPIS version used here, there exists a possibility to model the boom as a thin wire but how to use this functionality was not completely well understood by us at that time. So it is decided to approximate the wire boom as a cylinder by using an effective potential approach similar to that used in case of cubes. The complexity of meshing a thin wire and the number of elements required can be drastically reduced by such an approximation. For such a cylinder, the equivalent potential that represents the real wire boom potential at the cylinder radius has to be calculated. The potential field at radial distance from the wire boom for an infinite cylinder in vacuum is expressed as (*Engwall, et.al*^[8]):

$$\Phi(r) = \Phi \frac{\ln(r) - \ln(g\lambda_D)}{\ln(a) - \ln(g\lambda_D)} \quad (11.1)$$

where r is the radial distance from the wire boom (the equivalent cylinder radius in this case), a the radius of the wire boom and $g (> 1)$ a real number, which in the combined form $g\lambda_D$, defines the location at which the potential goes exactly to zero. Making a reasonable assumption that the potential goes to zero at about twice the Debye length (24 m; $g = 2$) for the present case, the real boom potential of 35 V would decay to 12.68 V at a radial distance of 1 m. So a cylinder of 1 m radius is modeled to represent the wire boom in the simulations. However, there is a slight drawback in such an approximation. One of the conditions for an enhanced wake formation is that the flow energy of the ions should be less than the electrostatic potential of the spacecraft (equation 5.5.b). In the tenuous mesosonic plasma conditions considered here, the ion flow energies have typical magnitudes around 10 eV (*Engwall, et.al*^[8]) and the thermal energy in our simulations is 2 eV. Hence by keeping a low potential of 12.68 V, a substantial fraction of the ion population would be then hitting on the cylinder rather than getting scattered around it. Such a scenario wouldn't happen in our case realistically and the approximation would fail. An option to avoid this is to reduce the cylindrical radius so that the potential of the equipotential cylinder would be higher. But this would in turn raise the number of elements in the computational domain

since smaller cells have to be provided. So to get rid of both the problems, the cylindrical potential is raised to 15 V, keeping the same radius. Using the same value of g as above, this corresponds to a spacecraft potential of 41.4 V rather than 35 V, which is higher than what would usually be expected for the density 0.20 cm^{-3} that we have used in the simulation. While this may introduce a slight overestimate of the wake effect, we decided to opt for this solution due to the limited amount of available time. A hemispherical surface of radius 1 m is attached to the cylinder ends to take account of the potential decay in the axial direction from the ends of the wire boom. The equivalent cylinder model is shown in figure 11.1.

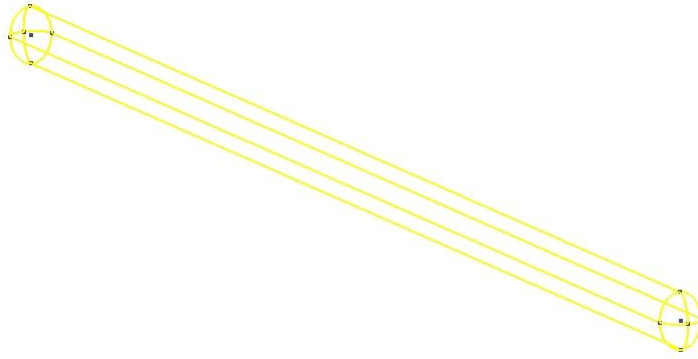


Figure 11.1: Cylindrical representation of the real wire boom

Two simulations are performed, one with a normal and the other a 45 degrees inclined alignment of boom relative to the flow. The plasma parameters are all kept the same as in spacecraft body (chapter 10) simulations, except that the potential is changed to 15 V, corresponding to 41.4 V spacecraft potential as noted above. The parameter settings are given in table 11.1.

| Parameters | Numerical values |
|------------------------------|--|
| Temperature (T) | 2.0 eV |
| Electron density (n) | 0.20 cm^{-3} |
| Debye length (λ_D) | 24 m |
| Potential (Φ) | 15.0 V |
| Cylinder size | (88×1) m plus 1 m end radius hemispheres |

Table 11.1: Simulation settings

11.2 Normal boom

A boom, when aligned normal to the flow direction, doesn't show any potential difference between its ends since the wake is symmetric. It is simulated for a qualitative check-out of the enlarged wake structure. A simulations box size of $200 \times 100 \times 200$ m is used for reducing the computational time but may not fully ensure minimum influence of the boundary conditions since the closest distance to the boundary is only $2 \lambda_D$ in the axial (Z) and normal (Y) directions. A hybrid boundary condition as used for cylinder is kept here also. An approximate of 3 million macro particles is employed for the simulation with a grid resolution of 1 m on the cylinder and 15 m at the boundaries. The ion wake density and potential as obtained from simulations are shown in figures 11.2 and 11.3.

The figures 11.2 and 11.3 show the relatively larger wake structure behind the booms, as compared to that behind the spacecraft body. The entire wake field is not captured due to the smaller simulation box but the ion density is very less affected by the boundary conditions and wake structure results necessarily from the potential of the boom. A little exaggeration from the real situation would have been occurred because of the larger potential kept on the cylinder. The same goes with the minimum potential in the wake of -0.5 V.

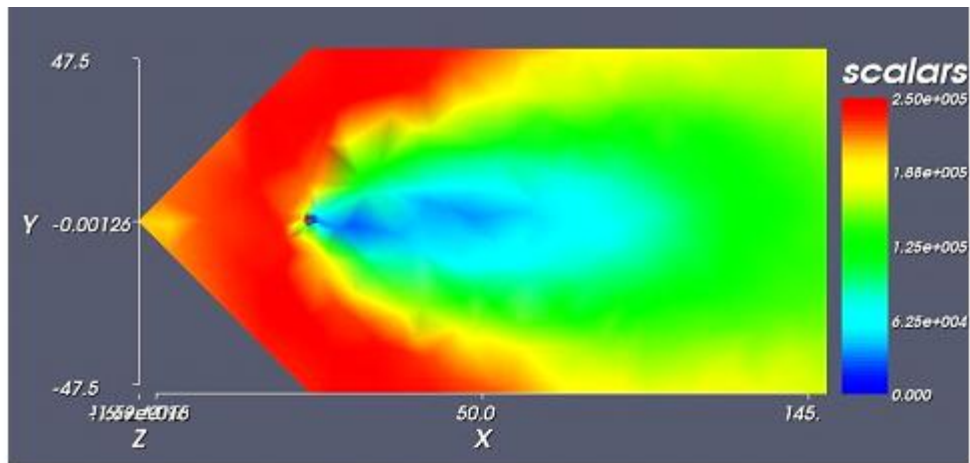
11.3 Inclined boom

In this, the same boom is aligned at 45 degrees relative to the flow in the XZ plane. The same closest distance to the boundary ($2\lambda_D$), as in the previous section, is maintained here also by providing a quadrilateral computational box with 45 degrees inclination of sides. For providing finer grids towards the boom with marginal increase in the overall elements, the mesh length on outer boundaries is reduced to 12 m. The ion density and potential obtained from simulations are depicted in figures 11.4 and 11.5.

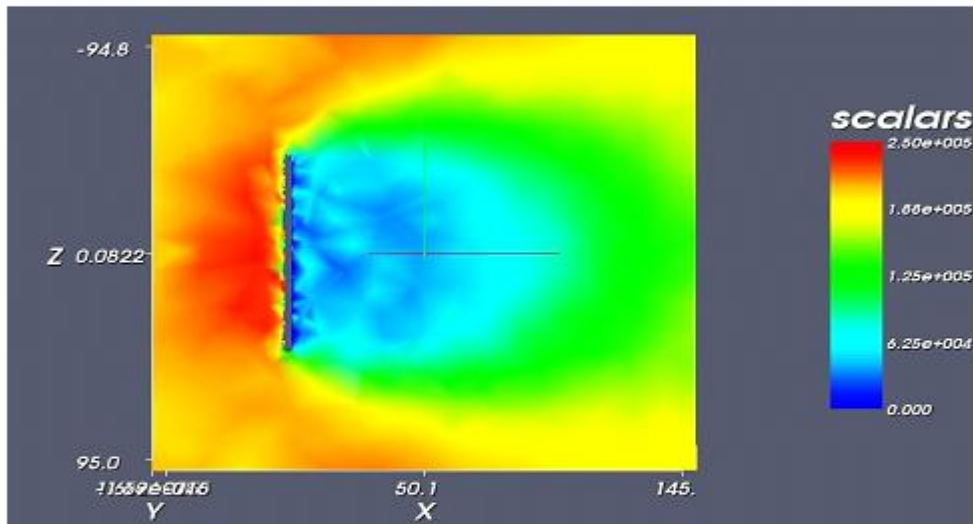
The ion density structures in 11.4 show that in all the planes, the boundary conditions only marginally affect the wake structure. This is expected as the ion ram energy is much larger than any potentials that can build up due to the space charge in the wake (order $\frac{kT_e}{q_e}$ or less), so that boundary conditions on the potential have little impact on the ion density. As expected, a clutter of ions can be observed on the forward side of the rearward end of the boom (figure 11.4.b). The equipotential surface on the forward part scatters sideways the incoming ions, which would then join the ions hitting on the equipotential surface developing from the rearward side. This is evident in XY plane (figure 11.4.c) also, where an unsymmetrical ion distribution with a high population around the rearward end is obtained.

To have quantitative analyses of the wake effects on the EFW measurements, we need to look in to the potential structure as given in figure 11.5. The negatively charged wake behind the boom attains a minimum value of -0.51 V, as per the simulations. The EFW probes extends 3 m outside the boom ends, which are at 35 V, with bootstrapped elements in between to shield away the influence of boom potential. Since we are using a hemispherical surface of 1 m radius at the ends, this would correspond to a probe distance of 2 m from the cylindrical boom ends. The potential difference between the forward and rearward probe locations give a value of around 229 mV, which agrees appreciably with the observed value at a 45 degree relative angle as given in *Engwall*^[3]. Thus for an 88 m boom, the wake would cause an apparent electric field of 2.6 mV/m in the EFW measurements. However, this would be larger in the real situation because the wake structure is further enlarged due to the spinning of the spacecraft. The observational data in figure 6 of *Engwall*^[3], agrees with this conclusion and it shows that an average apparent field of 3-4 mV/m is experienced.

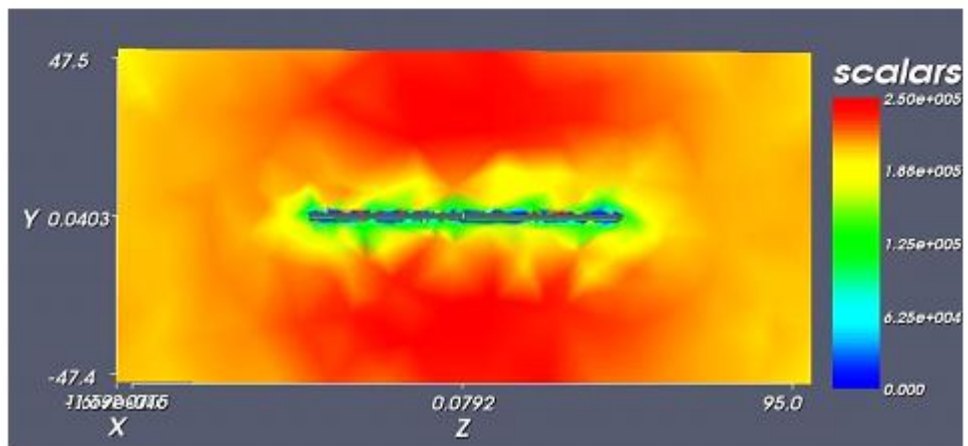
Another interesting feature is the electron density as shown in figure 11.6. A conglomeration of electrons around the boom is due to positive potential of the boom as well as the high thermal velocity of electrons. Also shown is a depletion region when compared to the overall electron structure in the wake. This region corresponds to the boundary of the Debye shielding where charge neutrality prevails predominantly.



(a): Ion density in XY plane (Grid points in m)

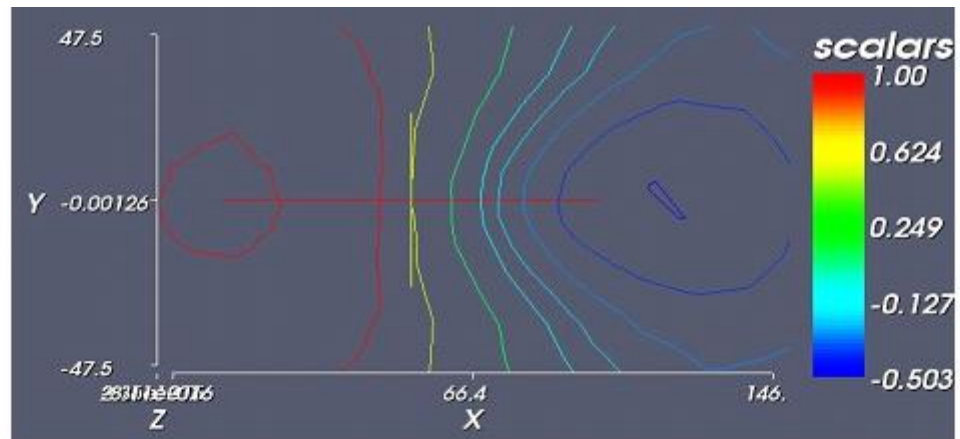


(b): Ion density in XZ plane (Grid points in m)

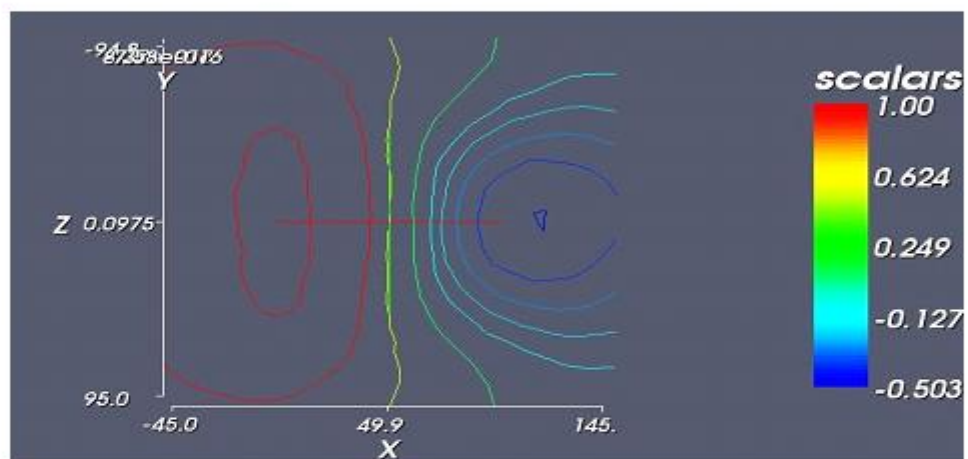


(c): Ion density in YZ plane (Grid points in m)

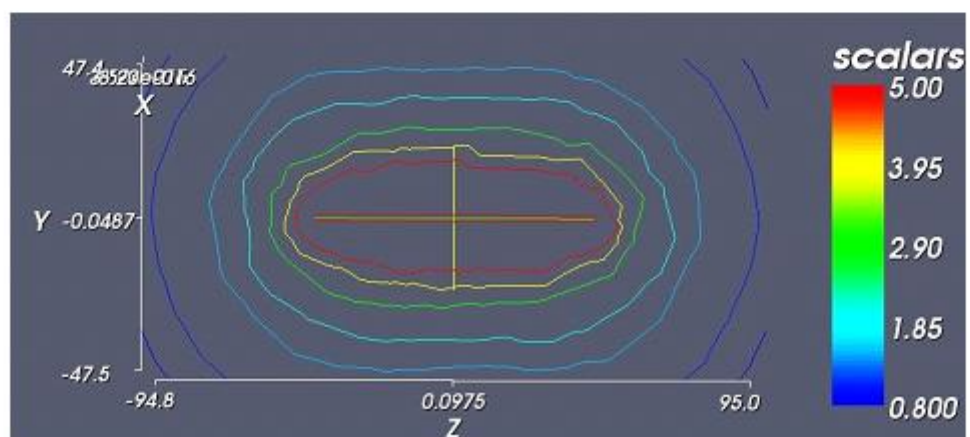
Figure 11.2: Ion density around the normal boom in various planes



(a): Potential in XY plane with a minimum value of -0.5 V (The equipotential contours are drawn for $-0.5, -0.4, -0.3, -0.2, -0.1, 0.1, 0.5, 1$ and 5 V)

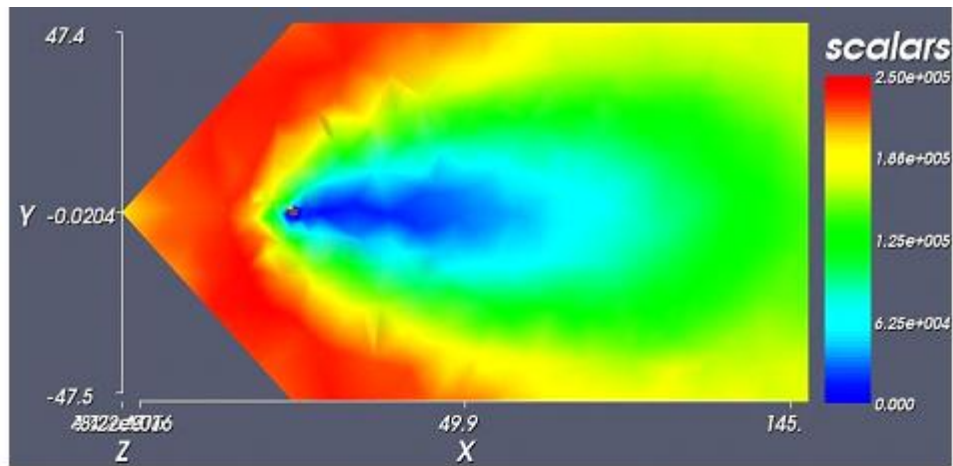


(b): Potential in XZ plane with a minimum value of -0.5 V (The equipotential contours are drawn for $-0.5, -0.4, -0.3, -0.2, -0.1, 0.1, 0.5, 1$ and 5 V)

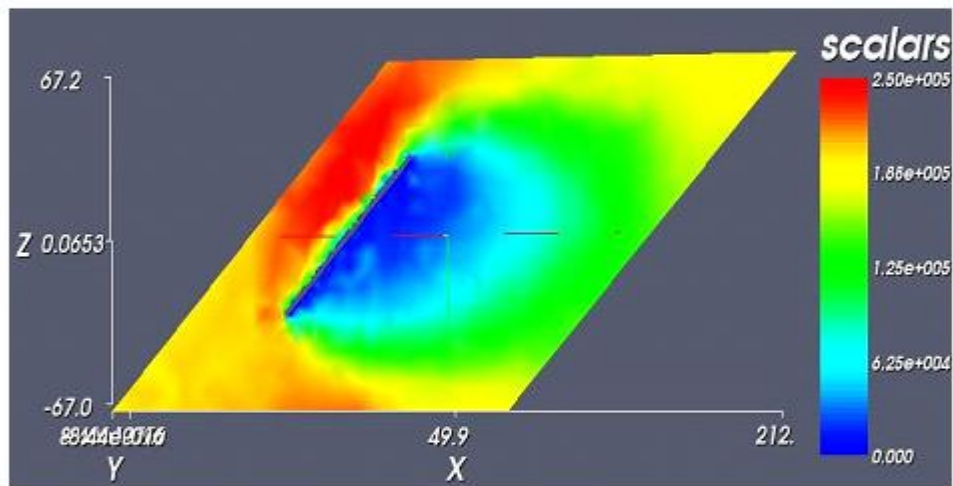


(c): Potential in XY plane with a minimum value of 0.8 V (The equipotential contours are drawn for $0.8, 1, 1.5, 2, 3, 4, 5$ and 15 V)

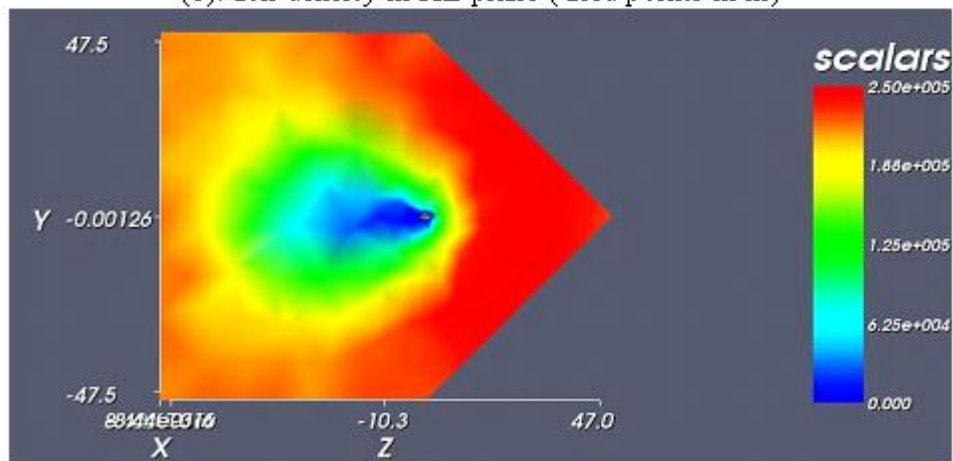
Figure 11.3: Plasma potential around the normal boom in various planes



(a): Ion density in XY plane (Grid points in m)

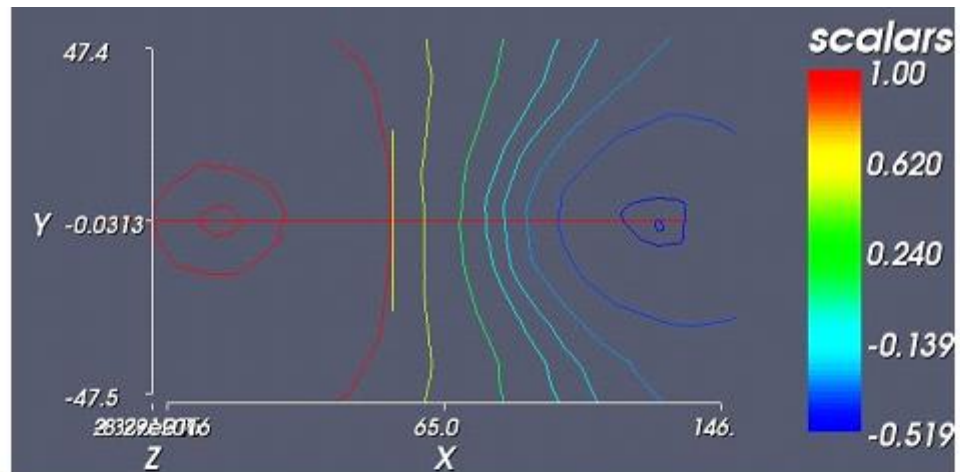


(b): Ion density in XZ plane (Grid points in m)

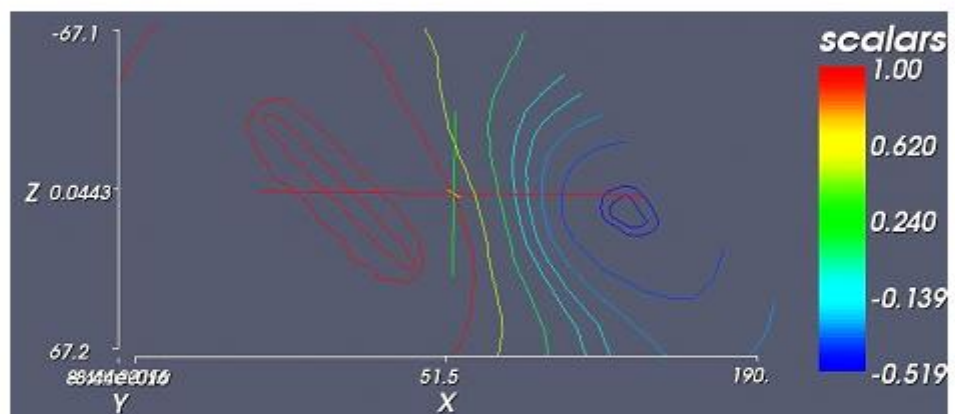


(c): Ion density in XY plane (Grid points in m)

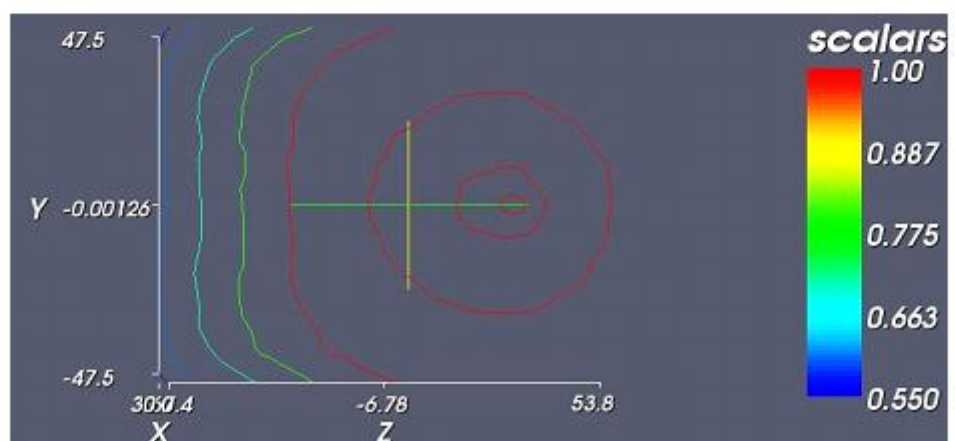
Figure 11.4: Ion density around the inclined boom in various planes



(a): Potential in XY plane with a minimum value of -0.51 V (The equipotential contours are drawn for $-0.51, -0.4, -0.3, -0.2, -0.1, 0.1, 0.5, 1, 5$ and 10 V)



(b): Potential in XZ plane with a minimum value of -0.51 V (The equipotential contours are drawn for $-0.51, -0.4, -0.3, -0.2, -0.1, 0.1, 0.5, 1, 5$ and 10 V)



(c): Potential in YZ plane with a minimum value of 0.8 V (The equipotential contours are drawn for $0.8, 1, 1.5, 2, 3, 4, 5$ and 10 V)

Figure 11.5: Plasma potential around the inclined boom in various planes

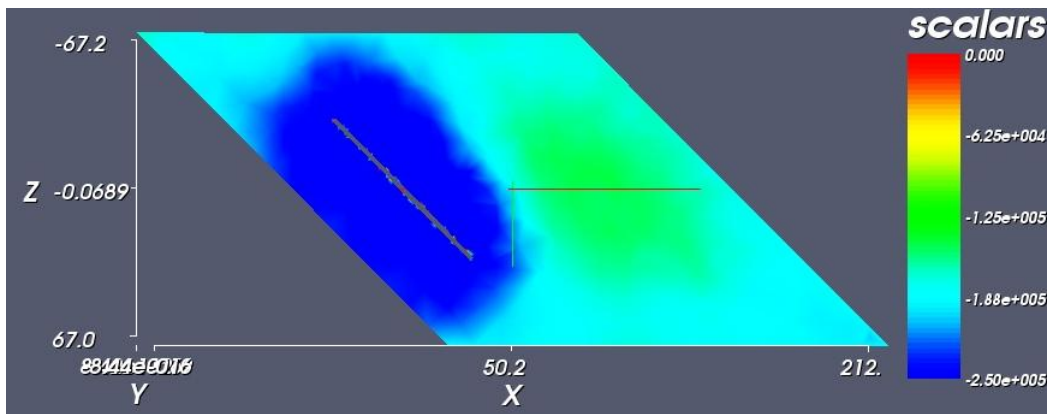


Figure 11.6: Electron density around the inclined boom in XZ plane

Chapter 12

Conclusions

The results presented in the previous chapters have consolidated the ability of SPIS in modeling spacecraft-plasma interactions. The main problem associated with EFW measurements have been the presence of a spurious electric field due to the wake formation in tenuous flowing plasmas in the magnetospheric tail lobes. Since the ion kinetic energy is much lower than the positive spacecraft potential (due to photoelectron emission) in tenuous mesosonic plasma, an ion wake is formed behind such a charged obstacle. Instead of hitting on the spacecraft, the ions would flow around an equipotential surface, corresponding to the ion flow kinetic energy, resulting in an enlarged wake. This modifies the free stream plasma potential which the EFW probes are supposed to measure. Through the simulations we have been able to quantitatively estimate the errors induced on the measurements by the wake formation.

Even though a thorough analysis is done on both spacecraft body as well as booms, it would be better to simulate the plasma flow over full spacecraft geometry. Such an approach couldn't be performed within the stipulated time of this project. So the present work deserves more to be done in that direction. Above all, in the used as well as new versions of SPIS, the possibility to model a thin wire exists so that instead of an effective potential approach for the boom we can model it as a thin wire. Such a model would be well closer to the real geometry, and obviously a better result can be obtained. However, the modeling of a thin wire is little tricky in the sense that it cannot be modeled as a lone entity but has to be part of a surface boundary. It can then be grouped as a physical edge while defining the physical entities. The documentation (*Roussel, et.al*^[6]) associated with the SPIS version used here doesn't emphasis on the modeling of such a wire but rather gives few details on the theoretical aspects. It could be included in the recent versions of SPIS.

Another feature of interest would be to determine the complete wake structure. For all the simulations, we have employed computational boxes with sizes just sufficient to fully capture the larger negative potentials behind the structure. Such an approach is followed to reduce the computational time. Apart from the reduced wake size, the boundary conditions never affected the wake potential, as it thought before the simulations. The wake structure was predominantly determined by the source potential (body or boom). Further simulations could be performed in this line as well, if the matter of interest is on the wake size. However, from the present project perspective, the emphasis was more on the potential perturbation at the EFW probe location and this lies well within a radius of 47 m from the spacecraft's centre.

For all the simulations we have neglected the magnetic field as well as the photoelectron emission. The exclusion of magnetic field would have caused some over estimation of electron densities in the wake because the electron gyro radius is comparable to the Debye length scale of the simulated plasma flow. The photoelectron emission could significantly alter the wake characteristics by filling it with photoelectrons rather than that of the incoming ones,

though the high spacecraft potential should imply that only few photoelectrons reach the wake. Also cross exchange can also happen such that the electrons emitted from the body would be collected by the booms and vice versa. So for a more realistic simulation, it is necessary to include these effects as well and both these can be modeled in the SPIS version used here.

One of the main advantages of SPIS, when compared with PicUp3D has been the use of an adaptive (non-uniform) grid approach, thereby considerably reducing the simulation time and also enacting the possibility to model complex geometries. However, the advantage, to a certain extent, is shadowed by the issues pertaining to the average PIC and cell volume ration, as discussed in chapter 7. Apart from that, the ease in modeling complex geometries has eliminated the need for an effective potential approach, as done with PicUp3D simulations. The adaptive grids have enabled us to provide finer grids near the source, hence reducing the over estimation of potentials and at the same time with little increase in the overall cells in the domain.

In the initial simulations done to check the effect of boundary conditions, it showed that the influence of boundary conditions on the wake structure is marginal as evident in the almost identical results obtained for both Dirichlet and Neumann conditions. A difference would have shown up if a further smaller computational domain had been used, but in SPIS it again depends on the order of preference we use while defining the boundaries. A higher preference for the body or boom surface implies no constraints would be imposed by the boundary conditions on the potential of source. The chosen hybrid boundary condition, with Dirichlet at flow entrance and Neumann elsewhere, works well such that it allows the choice of a smaller computational box and the potential on the boundary would be interpolated from the potential structure inside the box.

Bibliography

- [1] Roussel J-F. Rogier F. Volpert D. Forest J. Rousseau G. Hilgers A. Spacecraft plasma interaction software (SPIS) - numerical solvers-methods and architecture. In *9th Spacecraft Charging Technology Conference*, Tsukuba, Japan, April 2005. JAXA.
- [2] Tribble A.C. *The Space Environment: Implications for spacecraft design*. Princeton University Press, New Jersey, 1995.
- [3] Engwall E. Numerical studies of spacecraft plasma interaction: Simulations of wake effects on the cluster electric field instrument EFW. IRF scientific report 284, Swedish Institute of Space Physics, Uppsala, Sweden, February 2004.
- [4] Engwall E. *Cold magnetospheric plasma flows: Properties and interaction with spacecraft*. Licentiate thesis, Swedish Institute of Space Physics, Uppsala, Sweden, March 2006.
- [5] Roussel J-F. Hilgers A. Thiebault B. Forest J. Engwall E. Test and validation of a new spacecraft plasma interaction software, SPIS. In *9th Spacecraft Charging Technology Conference*, Tsukuba, Japan, April 2005. JAXA.
- [6] Roussel J-F. et al. *SPIS documentation*. ONERA/ Artenum/ ESA-ESTEC, version 3.6 edition, 2006.
- [7] Remacie J-F. Gauzaine C. *Gmsh: a three-dimensional finite element mesh generator with built-in pre and post processing facilities*, version 1.65 edition, May 2006.
- [8] Engwall E. Eriksson A.I. Forest J. Wake formation behind positively charged spacecraft in flowing tenuous plasmas. *Physics of Plasmas*, 13(062904), June 2006.
- [9] Kallenrode M-B. *Space Physics: An introduction to plasmas and particles in the Heliosphere and Magnetospheres*. Springer-Verlag, Berlin-Heidelberg, 2 edition, 2001.
- [10] Eriksson A.I. Khotyaintsev Y. Lindqvist P-A. Spacecraft wakes in the solar wind. In *Proceedings of the 10th International Spacecraft Charging Technology Conference (SCTC-10)*. CNES, 2007.
- [11] Dendy R. *Plasma Physics: An introductory course*. Cambridge University Press, Cambridge, 1993.
- [12] Roussel J-F. Forest J. Hilgers A. Thiebault B. Jourdain S. SPIS-UI, a new integrated modelling environment for space applications. In *9th Spacecraft Charging Technology Conference*, Tsukuba, Japan, April 2005. JAXA.

Appendix A

Simulation Settings and Procedures

The following procedures explain the simulation of a cylinder in cold, tenuous plasma using SPIS. The size of the cylinder is of same dimension as that of the Cluster body. Only the simulation part in using SPIS-UI is explained here. The geometry creation and group settings are done in Gmsh outside SPIS and the geometry is then simply loaded. The entire computational domain is shown in figure A.1.

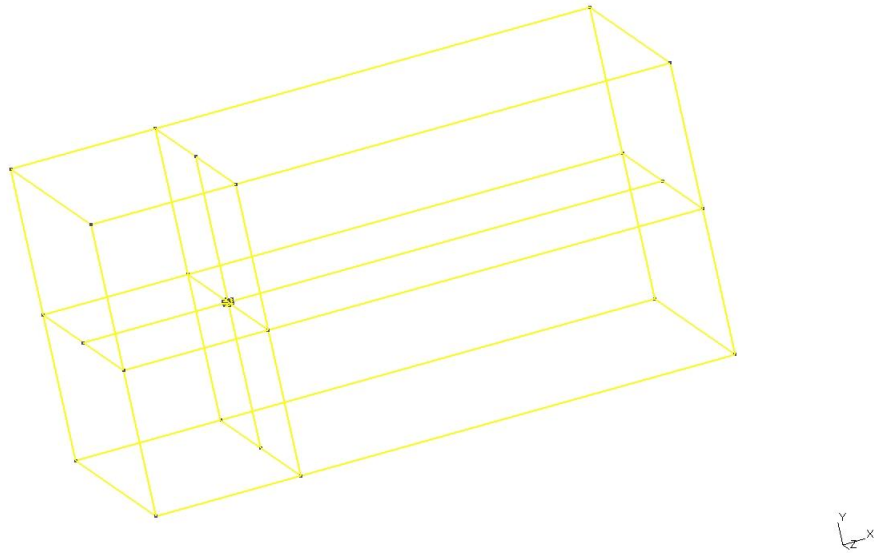


Figure A.1: Cylinder and far field boundaries

The physical group settings and required plasma boundary conditions are as follows:

- Physical Surface Group 1: Left end of the simulation box (Dirichlet BC)
- Physical Surface Group 2: Top, Bottom and Sides of the simulation box (Dirichlet BC)
- Physical Surface Group 3: Cylinder surface (Dirichlet BC)
- Physical Surface Group 4: Right end of the simulation box (Neumann BC)
- Physical Volume Group: The entire volume between the cylinder and outer box (Plasma Volume BC)

The simulation parameters are given in table A.1 (All units are in m):

| Feature | Data |
|---|-----------------------|
| Cylinder dimensions | 2.9d×1.5h |
| Characteristic length of mesh points on the cylinder | 1 |
| Simulation box dimensions | 200×100×100 |
| Characteristic length of mesh points on the simulation box boundaries | 100 |
| Number of macro particles | 4 million |
| Number of cells | 32685 |
| Average number of PIC | 122 |
| Ion velocity | 44 m/s |
| Duration of simulation | 0.005 s |
| Temperature | 2 eV |
| Cylinder potential | 35 V |
| Plasma density | 0.20 cm ⁻³ |

Table A.1: Simulation parameters

A.1 Before starting SPIS

The very first thing to do is to make two folders, say Cylinder and Cylinder Results, the latter one to save the project files and the other to save the results.

- Copy the geometry file, say cylindergeometry.geo, into the folder Cylinder

Now we can start the SPIS. Make sure to give the spinner-nT command (in Linux as well as Free BSD machines) before executing the SPIS, if the command is executed from a local host. So the connection between the local and server remains intact as long as the simulation runs.

A.2 After starting SPIS

A.2.1 Loading the geometry

- In the SPIS window, top left corner click File→New Project. Select folder Cylinder and click OK
- Click Open CAD (the second line of command buttons in SPIS window). Select cylindergeometry.geo in the folder Cylinder and click OK. This will only provide a reference to that geometry, but wont load it into SPIS.
- Click Modeller. This will open Gmsh GUI and you can see the geometry in that. If not click Open in the Gmsh command window and select the same geometry file.
- In the Gmsh command window click Tools→Visibility.
- In the Visibility sub window change the Elementary option to Physical on the left side drop menu. The list will then change to the physical entities instead of the geometrical entities in the Elementary option.
- Click one of them and then Apply. We can then see the selected physical group in the GUI. Do the same with all the elements in the physical list so as to make sure that the physical groups are properly allocated.

In this Gmsh window, we can edit the geometry file through the Edit button. If any changes are made, it has to be saved and structure reloaded in Gmsh by clicking Reload button. If we are making any additions using Gmsh GUI, then it is automatically saved.

- Exit Gmsh by clicking File→Quit.
- Click Load CAD button in SPIS window.

Now the geometry will be loaded in to SPIS. While executing the commands keep track of the logs window as it shows the termination of execution. Then proceed with the next command. If another command is tried before full termination of the previous ones, SPIS may get stuck.

A.2.2 Properties definition

- Click Prop button (By this all the default properties from SPIS library would be called). We can either select the default properties for our boundaries in the simulation or edit them according our needs and attribute them to the physical groups.
- Click on Properties (first line of commands)→Edit Properties→Material Editor. The material editor window pops up now.
- In the Material editor window there are some numbers given on the left side which correspond to different materials and properties. In that click on 0. On the right side of the window the Name, Description and Data of that material will then be shown.
- In the Data, click on 4(PhotoEmis) and then on the right most side click Modify. A DataEditor window will then pops up. In that turn the Value to 0 and click OK. Here we are turning off the photoemission flag. This actually will be overridden depending on what we specify for interactions in the global parameter settings. So we have to keep the interaction flags off there also (It is off by default in global settings).
- Do the same for 5(ElecSecEmis) and 6(ProtonSecEmis) in the Material editor window.
- Finally click OK on the Material Editor window.

Now we are done with editing the material properties according to our requirements in the simulation.

- Click on Properties→Edit Properties→Plasma Editor. The plasma editor window will then pops up.
- In the Plasma editor window, choose the number 300. Like in the material editor the right side of the window shows the descriptions for Boundary Default that represents Fourier conditions. We can change this to pure Dirichlet condition as required for our boundaries on the left end and on the top, bottom and sides.
- In the Data list click 5(BdDiriFlag)→Modify
- In the popped up data editor window turn Local to 2 (which represents the surface; 0 for nodes, 1 for lines and 3 for volume) and Value to 1 (which means we are initializing a Dirichlet condition) and then click OK
- In the Data list click 6(BdDiriPot)→Modify
- In the popped up data editor window turn Local to 2 (the default Value is 0.0 which now represents a 0 potential on the boundary surfaces) and click OK
- In the Data list click 7(BdFourFlag)→Modify
- In the popped up data editor window turn Value to 0 (which represents turning off the default Fourier conditions) and click OK

- Now click the number 211 in the Plasma Editor window and as before the right side then shows the corresponding boundary condition descriptions. In the Name and Description change the default potential 20V to 35V. This is to identify the potential while attributing it to groups.
- In the Data List click on 7(SCDiriFlag)→Modify. In the data editor window change the Local to 2 and click OK
- In the Data List click on 8(SCDiriPot)→Modify. In the data editor window change the Local to 2 and Value to 35.0. Then click OK.
- Click number 320 in the Plasma Editor window. This is the default Neumann BC implementation.
- In the Data on right hand side click 9(BDFourValue)→Modify. Change Local to 2 and click Ok.
- Click 10(IncomPart)→Modify. Change Value to 1 and click OK. This is done to make it an open boundary where the particles can come in and go out.
- Click 11(OutgoPart)→Modify. Change Value to 0 and click OK. This along with the previous step makes the boundary an open one with the particles can freely come in go out but they are not reflected from the boundaries.
- Finally, click OK in plasma editor window.

Now we are done with editing all the plasma properties.

At first we have loaded the geometry in to SPIS. Then we called the default material and plasma properties in the library. But these default values are not the ones we need for our simulations. So we edited some of them according to our requirement so that we can attribute those to our boundaries.

A.2.3 Properties attribution

- Click on Edit Grps button (on the lower line of command buttons). The groups actually refer to the physical groups which have been specified while creating the geometry and as mentioned before. For e.g., we need to specify the boundary conditions on the left, top, bottom and sides of the simulations box as Dirichlet so we grouped them in one physical group and assign the Boundary condition to that group.
- In the Group Editor window click on 1. This surface corresponds to the left end boundary of the simulation box. So it doesn't have any material or electric properties. It has only plasma property which has a Dirichlet condition of zero potential. So turn the Material and Elecnode to None and Plasma to Boundary, default.
- Now click on surface 2 (top, bottom and sides of simulation box) and do the same procedure as above
- Click on surface 3 (the spacecraft surface). This surface has material, electric and plasma properties. The plasma potential has a value to 35 V and electric node is has to be set to ground. Change the material to ITO default, Elecnode to Spacecraft ground (Elecnode-0) and plasma to Spacecraft pot=35.
- Click on surface 4 (the left end of simulation box). This surface is also like 1 and 2 but the plasma boundary condition has to be set to Neumann. So change material and Elecnode to None and Plasma to Boundary symmetry

- Click on 5 which is the volume. Change Material and Elecnode to None and Plasma to Plasma model in volume, default.
- The groups 6-8 are default groups. Change all the parameters to these groups to None.
- Click OK in the Group Editor window.

A.2.4 Meshing the geometry and group conversion

- Click the 3D mesh button. SPIS would then call the Gmsh external tool and mesh the structure. It takes a while before the meshing is complete.
- Click Convert Grps. This command would then convert the physical groups to mesh groups.
- Click on Fields. This would then attribute the data we gave to the boundaries to the corresponding mesh groups.

A.2.5 Global parameter settings

A brief description about the global parameter settings are given in section 7. Here only those values, which are to be changed for this simulation, are mentioned in the order given in SPIS. Make sure of decimal points as type may be important.

Click on Global Parameters and a pop up screen will open. The following values are to given there:

| Parameter | Data |
|--------------------------|---------------------------------|
| ion Density | 200000.0 |
| ionVx | 44000.0 |
| avPartNbPerCell | 122.0 |
| electron Temperature | 2.0 |
| linear Poisson | 1 |
| ion Temperature | 2.0 |
| duration | 0.005 |
| electron Density | 200000.0 |
| initPot | 35.0 |
| electronDistrib | PICVolDistrib (write like this) |
| electricCircuitIntegrate | 0 |

Table A.2: Global parameters

Now click *saveandquit* and then *UItoNum* button for converting the UI data structure to that of Num. Then click the *RunSolver* command. If everything ok the solver should start running now. The time for convergence depends on the computer and memory allocation. It took 2.5 - 3 days on dual processor computer with 2.5 GB RAM allocation.

A.2.6 Post processing

There are 3D viewing tools integrated with SPIS, Paraview and Cassandra. Both these tools require the output files in VTK format for post processing. Here we will not explain the usage of these tools, but only the generation and saving of VTK files from the outputs. As an example, we check the ion density.

- Click on Fields→DataFields Manager. A field manager window then pops up.

- In the drop down menu, click ion density. The ion density at the final integration time has to be chosen.
- Turn View on option to Cell. This is because we need to obtain the values on cells over the surface.
- Click Build Grid.
- Click Save to VTK. The file will be saved in a temporary exchange folder which can then be transferred to our folder, Cylinder Results.

The same procedure can be followed for other members in the drop down list. Close the manager window when done with all the required output parameters.

A.2.7 Saving the project file

It is a good practise to save the project files after simulation. This will be beneficial if we want to check the settings in the future or re-run the simulation. In that case we can simply load the project file into SPIS, re-mesh and run the simulation.

- Click File→Save project.
- In the popped up sub window, double click the folder Cylinder. In that folder, make a subfolder with name say Project. Select that folder and click Select Directory in the sub window. All the project files, which include the mesh, geometry, properties and global settings, will then be stored in Project. If we want to re-run the simulation, after opening SPIS, just click File→Open project.